A hybrid analysis method for displacement-monitored segmented circular tunnel rings

Jiao-Long Zhang [a,b], Christoffer Vida [a], Yong Yuan [b], Christian Hellmich [a], Herbert A. Mang [a,b], Bernhard Pichler [a,*]

[a] Institute for Mechanics of Materials and Structures, Vienna University of Technology (TU Wien), Karlsplatz 13/202, A-1040 Vienna, Austria
[b] College of Civil Engineering, Tongji University, Siping Road 1239, 200092 Shanghai, China

ABSTRACT

Segmented tunnel rings exhibit load-induced interfacial dislocations. In order to facilitate structural analysis, a hybrid method is developed and applied to a real-scale test of a segmented tunnel ring. Point loads, imposed on the tested ring, and measured interfacial discontinuities serve as input for the analysis. Moreover, the method accounts for the structural behavior of the individual segments by means of newly derived transfer relations. They represent analytical solutions of the first-order theory of slender circular arches, exhibiting constant cross-sectional properties. The tool for the development of this basically well-known theory is the principle of virtual power. Its involvement is motivated by the possibility of a mechanically consistent derivation of relations, some of which have been used for a long time without analyzing their scientific background. The validity and the usefulness of the transfer relations follow from a comparison of newly derived solutions with (i) alternative analytical solutions, (ii) Finite Element solutions, and (iii) experimental data. The computational efficiency and the usefulness of the developed hybrid method are demonstrated by structural analysis of a segmented tunnel ring. It provides valuable insight into the load-carrying behavior of the tested structure without the need to describe the nontrivial behavior of segment-to-segment interfaces.

© 2017 The Authors. Published by Elsevier Ltd. This is an open access article under the CC BY-NC-ND license (http://creativecommons.org/licenses/by-nc-nd/4.0/).

1. Introduction

The motivation for the present paper is structural analysis of a real-scale experiment of a segmented tunnel ring, tested at Tongji University [1], see Fig. 1. 24 hydraulic jacks imposed concentrated loads on the structure, simulating non-uniform ground pressure. During the stepwise loading process, monitoring instrumentation was used to measure convergences as well as discontinuities at segment-to-segment interfaces, i.e. relative rotation angles and displacement jumps in the radial and tangential direction. Both, point loads and interfacial dislocations result in discontinuities of static and kinematic variables. They render structural simulations a challenging task.

The complex contact behavior of segment-to-segment interfaces depends on many factors including their geometric layout, the potential use of prestressed connecting bolts, the stresses acting in the contact zone, as well as potential dislocations and relative rotation angles. This was the motivation for several testing

series, in which interfaces were subjected to normal forces and bending moments [2,3] or to normal and shear forces [4]. Corresponding models for the nonlinear interfacial behavior include analytical approaches [5–8] and numerical approaches, where the interfacial regions are modeled in great detail [9,10].

The structural behavior of segmented tunnel rings strongly depends on the complex interface behavior. This was the motivation for many structural experiments [11–14,1]. As for the corresponding structural analyses, several approaches exist. Interfaces were simulated as perfect hinges [15]. Closed ring models with reduced moments of inertia at the locations of interfaces were developed [16–19]. Interfaces were modeled explicitly based on rotational springs [20–23] and on systems of springs, allowing for both dislocations and relative rotation angles [24,25]. If realistic *nonlinear* interfacial behavior is taken into account, an incremental-iterative solution scheme is required even if the reinforced concrete segments exhibit linear elastic material behavior. This provides the motivation for the present study.

The aim of the present work is to establish a hybrid method for displacement-monitored segmented tunnel rings. This is inspired by existing hybrid methods, developed for structural analysis of

Fig. 1. Setup of the real-scale experiment of a segmented tunnel ring at Tongji University [1].

displacement-monitored shotcrete shells, used as linings in the New Austrian Tunneling Method, see, e.g. [26–29]. Herein, the word "hybrid" refers to the combination of *measurements* and analytical or numerical *computations* in structural mechanics. In the present context, *measured* interfacial discontinuities will be used (together with prescribed point loads) as input for the *computational* structural analysis. This eliminates the interfacial nonlinearities, and thus simplifies the structural analysis significantly. In addition, the structural behavior of the individual segments will be accounted for by means of analytical solutions of the small strain ("first-order") theory for slender circular arches with constant cross-sectional properties. Such transfer relations are appealing because they are capable of considering discontinuities of static and kinematic variables, for example, the ones resulting from point loads and interfacial dislocations, in a straightforward manner.

The present paper is organized as follows. In Section 2, the analyzed experiment on a segmented tunnel ring is described. Section 3 is devoted to the derivation and an exemplary validation of transfer relations, representing analytical solutions of the first-order theory for slender circular arches with constant cross-sectional properties. As for the validation, the transfer relations are applied to a two-hinged arch, subjected to a point load and to a three-hinged arch, subjected to dead load. Results obtained with the help of the derived transfer relations are compared with alternative analytical solutions obtained by the unit force method, results from Finite Element simulations, and experimental data.

Section 4 is devoted to the application of the transfer relations to the aforementioned hybrid analysis of a displacement-monitored experiment on a segmented tunnel ring. In the discussion in Section 5, (i) the reason for the unsymmetric structural response under symmetric external loading is explained, (ii) the question whether the tested segmented tunnel ring may be treated as a slender arch is answered, and (iii) the benefits from the presented hybrid approach are highlighted. Section 6 contains conclusions drawn from the presented study. Appendix A is devoted to the first-order theory of slender circular arches. The tool for the development of this basically well-known theory is the principle of virtual power. Its involvement is motivated by the possibility of a mechanically consistent derivation of relations, some of which have been used for a long time without analyzing their scientific background. Appendix B contains an analytical solution of an arch problem based on the unit force method. Appendix C contains a list of symbols.

2. Data from a real-scale test on a segmented tunnel ring

In this section, data from a full-scale experiment of a segmented tunnel ring, tested at Tongji University [1], are presented (Fig. 1). The radius R of the ring was 2.925 m, see Fig. 2(a). It consisted of six reinforced concrete segments, named K, A, B, C, D, E. Their thickness, H, and axial length, B, were 35 cm and 1.2 m, respectively. Young's modulus of concrete, E_c, amounted to 43,478 MPa [30,31], the extensional stiffness EA amounted to 18,260 MN, and the bending stiffness EI amounted to 186 MNm². Compressive loading was imposed by 3 groups of altogether 24 hydraulic jacks, see Fig. 2(b). They simulated the action of non-uniform earth pressure. The available measurements included jack forces and the interfacial displacement/rotation discontinuities (Fig. 3), as well as the vertical and horizontal convergences, see Fig. 4. The present re-analysis of the test focuses on the first 4 load steps, during which the segments remained uncracked [1]. Thus, the mechanical behavior of the segments can be modeled by linear elasticity theory.

3. Transfer relations for circular arches

Consider a slender arch with constant radius R, extensional stiffness EA, and bending stiffness EI, subjected to radial and tangential distributed loads, q_r and q_φ (Fig. 5). The first-order theory for such an arch consists of the following basic equations; for their derivation see Appendix A. The displacement vector, **u**, and the cross-sectional rotation, θ, are given as
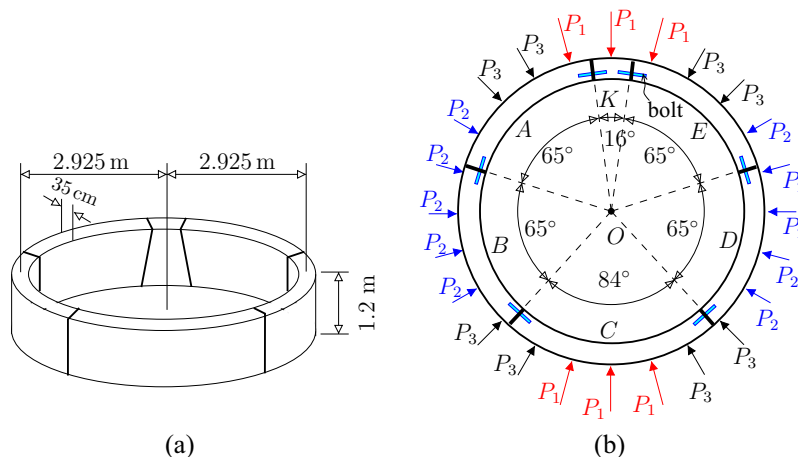

Fig. 2. (a) Geometric dimensions of the analyzed segmented tunnel ring, (b) composition of the ring and layout of the hydraulic jacks.
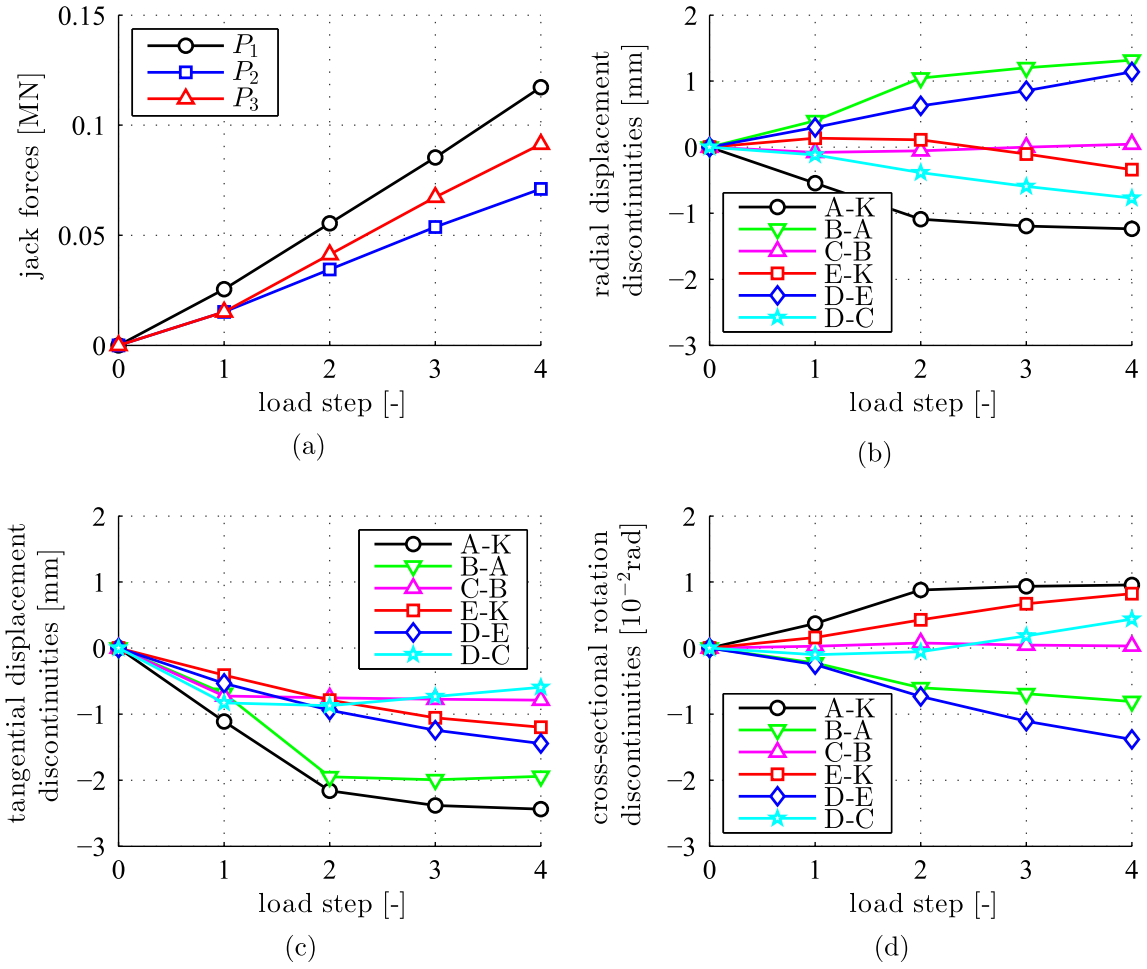
Fig. 3. Experimental data used as input for structural analysis: (a) imposed jack forces, (b) – (d) measured interfacial discontinuities of radial displacements, tangential displacements, and cross-sectional rotations; see [1].
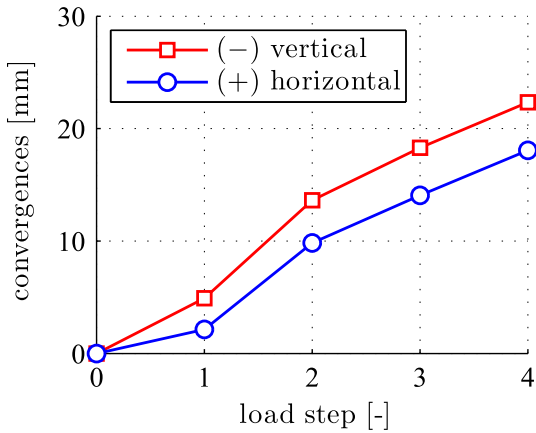

Fig. 4. Experimental data used for validation of the transfer relations: "+" and "−" refer to an increase and a decrease, respectively, of the initial diameter; see [1].

$$\mathbf{u} = u\,\mathbf{e}_r + \left[v - (r - R)\left(\frac{1}{R}\frac{du}{d\varphi} - \frac{v}{R} \right) \right]\mathbf{e}_\varphi, \tag{1}$$

$$\theta = \frac{1}{R}\frac{du}{d\varphi} - \frac{v}{R}, \tag{2}$$

where u and v denote the radial and tangential component of $\mathbf{u}$, respectively, r and φ stand for the radial and the tangential

coordinate, and $\mathbf{e}_r$ and $\mathbf{e}_\varphi$ symbolize the base vectors in the radial and the tangential direction (see Fig. 5). For linear elasticity the constitutive expressions for the normal force N and the bending moment M are given by [32,33]

$$N = EA\left(\frac{u}{R} + \frac{1}{R}\frac{dv}{d\varphi} \right), \tag{3}$$

$$M = -EI\left(\frac{1}{R^2}\frac{d^2u}{d\varphi^2} - \frac{1}{R^2}\frac{dv}{d\varphi} \right). \tag{4}$$

The equilibrium conditions read as [34]

$$-\frac{N}{R} + \frac{1}{R}\frac{dV}{d\varphi} + q_r = 0, \tag{5}$$

$$\frac{1}{R}\frac{dN}{d\varphi} + \frac{V}{R} + q_\varphi = 0, \tag{6}$$

$$\frac{1}{R}\frac{dM}{d\varphi} = V. \tag{7}$$

The distribution of normal stresses follows from [35]

$$\sigma_{\varphi\varphi} = \frac{N}{A} + \frac{M}{I}(r - R), \tag{8}$$

where A and I denote the cross-sectional area and the moment of inertia, respectively.

3.1. Stepwise solution scheme

In order to derive analytical solutions for N, V, M, u, v, and θ from Eqs. (2)–(7), a step-by-step integration strategy is developed. Combination of Eqs. (5) and (6) results in the following second-order differential equation for N

$$\frac{d^2N}{d\varphi^2} + N = R\left(q_r - \frac{dq_\varphi}{d\varphi}\right). \tag{9}$$

After solving Eq. (9), V follows from Eq. (6) as

$$V = -\frac{dN}{d\varphi} - Rq_\varphi. \tag{10}$$

Knowledge of the shear force enables solution of Eq. (7) for M

$$\frac{dM}{d\varphi} = R\,V. \tag{11}$$

Combination of Eqs. (3) and (4) results in the following second-order differential equation for u

$$\frac{d^2u}{d\varphi^2} + u = R\left(\frac{N}{EA} - \frac{MR}{EI}\right). \tag{12}$$

After solving Eq. (12), v follows from re-arrangement of Eq. (3), as

$$\frac{dv}{d\varphi} = \frac{NR}{EA} - u. \tag{13}$$

Finally, θ is obtained from Eq. (2) as

$$\theta = \frac{1}{R}\frac{du}{d\varphi} - \frac{v}{R}. \tag{14}$$

Subsequently, the described solution concept, see Eqs. (9)–(14), is applied to the following load cases: (i) an unloaded part of the arch, (ii) dead load, (iii) point loads, and (iv) interfacial discontinuities of kinematic variables.

Eqs. (9)–(14) represent a system of six linear differential equations in the six variables, N, V, M, u, v, and θ. This system is inhomogeneous because of the loading quantities q_r and q_φ. In load case (i), the load quantities q_r and q_φ are set equal to zero. Therefore, load case (i) refers to the derivation of the "homogeneous solution" of the system of differential equations. (9)–(14). The load cases (ii)–(iv), in turn, refer to the derivation of "particular solutions".

3.2. Solution for the unloaded part of the arch

For an unloaded arch, i.e. for $q_r = q_\varphi = 0$, the forces and the bending moment follow from the Eqs. (9)–(11) as

$$N(\varphi) = C_1 \sin\varphi + C_2 \cos\varphi, \tag{15}$$
$$V(\varphi) = -C_1 \cos\varphi + C_2 \sin\varphi, \tag{16}$$
$$M(\varphi) = -RC_1 \sin\varphi - RC_2 \cos\varphi + C_3. \tag{17}$$

It is useful to replace the mathematically motivated integration constants C_1, C_2, and C_3 by mechanically interpretable constants, chosen as the forces and the bending moment at the initial cross-section: i.e. as V_i, N_i, and M_i. The relations between these two sets of integration constants follow from Eqs. (15)–(17) as

$$V(0) = V_i \quad \Rightarrow \quad C_1 = -V_i, \tag{18}$$
$$N(0) = N_i \quad \Rightarrow \quad C_2 = N_i, \tag{19}$$
$$M(0) = M_i \quad \Rightarrow \quad C_3 = M_i + RN_i. \tag{20}$$

It is noteworthy that the validity of Eqs. (15)–(20) can be checked by means of equilibrium conditions, formulated for a part of the arch, ranging from the initial cross-section to the one defined by an arbitrary value of φ.

The kinematic state variables follow from the Eqs. (12)–(14) under consideration of the Eqs. (15)–(20) as

$$u(\varphi) = C_4 \cos\varphi + C_5 \sin\varphi + \frac{1}{2}\frac{R}{EA}[V_i\varphi\cos\varphi + N_i(\cos\varphi + \varphi\sin\varphi)]$$
$$+ \frac{1}{2}\frac{R^3}{EI}\left[V_i\varphi\cos\varphi + N_i(\cos\varphi + \varphi\sin\varphi) - \frac{2(M_i + RN_i)}{R}\right], \tag{21}$$

$$v(\varphi) = -C_4 \sin\varphi + C_5 \cos\varphi + C_6$$
$$+ \frac{R}{EA}\left[-\frac{1}{2}V_i(-\cos\varphi + \varphi\sin\varphi) + \frac{1}{2}N_i\varphi\cos\varphi\right]$$
$$+ \frac{R^3}{EI}\left[-\frac{1}{2}V_i(\cos\varphi + \varphi\sin\varphi) + N_i\left(\frac{1}{2}\varphi\cos\varphi - \sin\varphi\right) + \frac{M_i + RN_i}{R}\varphi\right], \tag{22}$$

$$\theta(\varphi) = -\frac{C_6}{R} + \frac{R^2}{EI}\left(V_i\cos\varphi + N_i\sin\varphi - \frac{M_i + RN_i}{R}\varphi\right). \tag{23}$$

Again, it is useful to replace mathematically motivated integration constants C_4, C_5, and C_6 by mechanically interpretable constants, chosen as the state variables at the initial cross-section, i.e. u_i, θ_i, and v_i. The relations between these two sets of integration constants follow from Eqs. (21)–(23) as

$$u(0) = u_i \quad \Rightarrow \quad C_4 = u_i + M_i\frac{R^2}{EI} + N_i\left(-\frac{1}{2}\frac{R}{EA} + \frac{1}{2}\frac{R^3}{EI}\right), \tag{24}$$

$$\theta(0) = \theta_i \quad \Rightarrow \quad C_6 = -\theta_i R + V_i\frac{R^3}{EI}, \tag{25}$$

$$v(0) = v_i \quad \Rightarrow \quad C_5 = v_i + \theta_i R + V_i\left(-\frac{1}{2}\frac{R}{EA} - \frac{1}{2}\frac{R^3}{EI}\right). \tag{26}$$
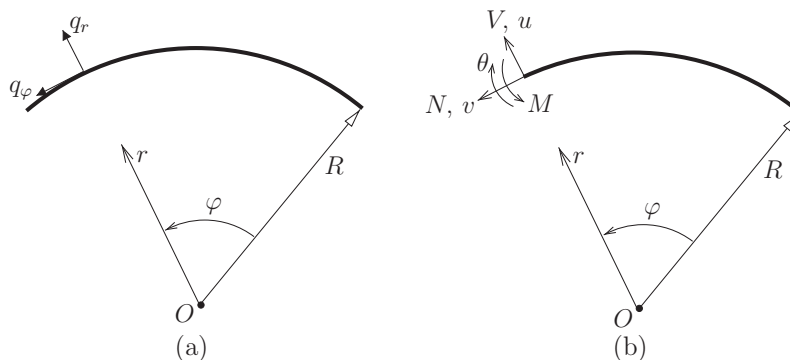
Fig. 5. (a) Circular arch of radius R, loaded by radial and tangential distributed loads, q_r and q_φ, in the r-φ plane (the distributions of q_r and q_φ are not shown), (b) displacements and internal forces at an arbitrary cross-section; u and v denote the radial and the tangential component of the displacement of the axis, θ is the cross-sectional rotation, and N, M, and V are the normal force, the bending moment, and the shear force, respectively (arrows point in positive directions).

Eqs. (15)–(26) refer to the homogeneous solution of the differential equations (9)–(14). Notably, the integration constants were introduced as the static and kinematic variables at the initial cross-section. Therefore, *homogeneous boundary conditions* must be considered in the following derivation of particular solutions of the inhomogeneous system of differential Eqs. (9)–(14).

3.3. Particular solutions for dead load

The dead load q is decomposed into its radial and tangential component, i.e. $q_r = -q\sin(\varphi + \beta)$ and $q_\varphi = -q\cos(\varphi + \beta)$, where β denotes the inclination angle of the initial cross-section, see Fig. 6. Corresponding particular solutions for static and kinematic variables are called *load integrals*. They are marked by the superscript *L*.

The particular solutions for the forces and the bending moment follow from the Eqs. (9)–(11). Considering the homogeneous boundary conditions $N^L(0) = 0$, $V^L(0) = 0$, $M^L(0) = 0$, the following relations are obtained:

$$N^L(\varphi) = Rq\varphi\cos(\varphi + \beta), \tag{27}$$

$$V^L(\varphi) = Rq\varphi\sin(\varphi + \beta), \tag{28}$$

$$M^L(\varphi) = R^2 q[\sin(\varphi + \beta) - \varphi\cos(\varphi + \beta) - \sin\beta]. \tag{29}$$

Analogous to the Eqs. (15)–(20), the validity of the Eqs. (27)–(29) can be checked by means of equilibrium conditions, formulated for a part of the arch, ranging from the initial cross-section to the one defined by an arbitrary value of φ.

The particular solutions for the kinematic state variables follow from the Eqs. (12)–(14). Considering the homogeneous boundary conditions $u^L(0) = 0$, $v^L(0) = 0$, $\theta^L(0) = 0$, the following relations are obtained:

$$u^L(\varphi) = \frac{R^2 q}{4EA}[\varphi^2\sin(\varphi + \beta) + \varphi\cos(\varphi + \beta) - \cos\beta\sin\varphi] + \frac{R^4 q}{4EI}[(\varphi^2 - 4)\sin(\varphi + \beta) + 3\varphi\cos(\varphi + \beta) + 2\sin\varphi\cos\beta + 4\sin\beta], \tag{30}$$

$$v^L(\varphi) = \frac{R^2 q}{4EA}[\varphi^2\cos(\varphi + \beta) + \varphi\sin(\varphi + \beta) - \sin\beta\sin\varphi] + \frac{R^4 q}{4EI}[(\varphi^2 - 8)\cos(\varphi + \beta) - 5\varphi\sin(\varphi + \beta) + (\sin\varphi - 4\varphi)\sin\beta + 8\cos\beta], \tag{31}$$

$$\theta^L(\varphi) = \frac{R^3 q}{EI}[\varphi\sin\beta + \varphi\sin(\varphi + \beta) + 2\cos(\varphi + \beta) - 2\cos\beta]. \tag{32}$$

3.4. Particular solutions for point loads

The point load P, acting at an arbitrary point of the arch, which is defined by the angle φ_p (Fig. 7), is decomposed into its radial and tangential component, P_r and P_φ. These components are introduced as limiting cases of distributed loads q_r and q_φ:

$$P_r = \lim_{\epsilon \to 0}\int_{\varphi_p - \epsilon}^{\varphi_p + \epsilon} q_r\,R\,d\varphi, \tag{33}$$

$$P_\varphi = \lim_{\epsilon \to 0}\int_{\varphi_p - \epsilon}^{\varphi_p + \epsilon} q_\varphi\,R\,d\varphi. \tag{34}$$

Both, $q_r(\varphi)$ in Eq. (33) and $q_\varphi(\varphi)$ in Eq. (34), are expressed by means of the Dirac function, defined as

$$\delta(\varphi - \varphi_p) = \begin{cases} 0 & \ldots\varphi \neq \varphi_p, \\ +\infty & \ldots\varphi = \varphi_p, \end{cases} \tag{35}$$

which satisfies

$$\lim_{\epsilon \to 0}\int_{\varphi_p - \epsilon}^{\varphi_p + \epsilon}\delta(\varphi - \varphi_p)\,d\varphi = 1. \tag{36}$$

The expressions for $q_r(\varphi)$ and $q_\varphi(\varphi)$ follow from multiplying Eq. (36) by P_r and P_φ, respectively, and comparing the resulting terms with Eq. (33) and Eq. (34), respectively, as

$$q_r = \frac{P_r}{R}\delta(\varphi - \varphi_p), \tag{37}$$

$$q_\varphi = \frac{P_\varphi}{R}\delta(\varphi - \varphi_p). \tag{38}$$

A point load results in discontinuities of both the normal force and the shear force at the load point. The bending moment is continuous but not smooth at such a point. This situation is described mathematically by means of the Heaviside function,

$$H(\varphi - \varphi_p) = \begin{cases} 0 & \ldots\varphi < \varphi_p, \\ 1 & \ldots\varphi \geqslant \varphi_p, \end{cases} \tag{39}$$

the derivative of which is equal to the Dirac distribution, i.e.

$$\frac{dH(\varphi - \varphi_p)}{d\varphi} = \delta(\varphi - \varphi_p). \tag{40}$$

The particular solutions for the forces and the bending moment follow from the Eqs. (9)–(11). Considering homogeneous boundary conditions, the following relations are obtained:

$$N^L(\varphi) = \left[P_r\sin(\varphi - \varphi_p) - P_\varphi\cos(\varphi - \varphi_p)\right]H(\varphi - \varphi_p), \tag{41}$$

$$V^L(\varphi) = -\left[P_r\cos(\varphi - \varphi_p) + P_\varphi\sin(\varphi - \varphi_p)\right]H(\varphi - \varphi_p), \tag{42}$$

$$M^L(\varphi) = -R\left\{P_r\sin(\varphi - \varphi_p) + P_\varphi\left[1 - \cos(\varphi - \varphi_p)\right]\right\}H(\varphi - \varphi_p). \tag{43}$$

Analogous to the Eqs. (15)–(20), the validity of the Eqs. (41)–(43) can be checked by means of equilibrium conditions, formulated
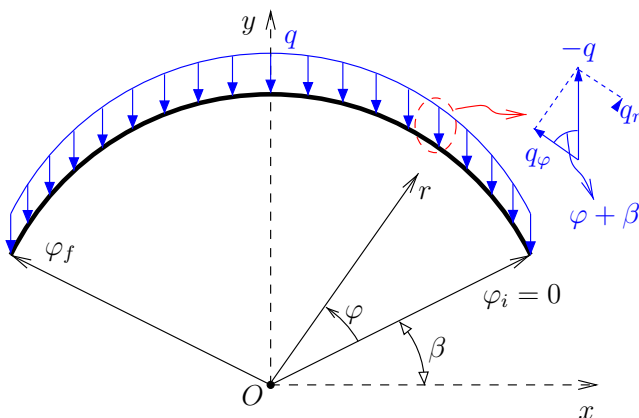

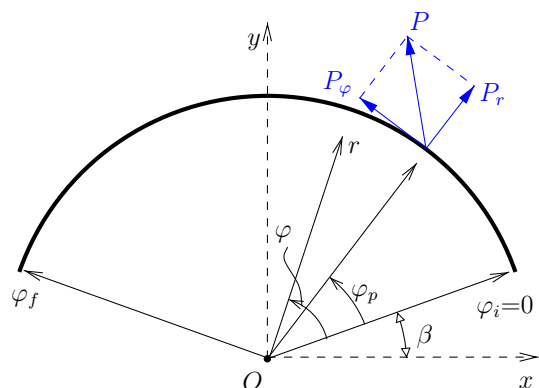**Fig. 6.** Decomposition of q into q_r and q_φ.

Fig. 7. Point load P at $\varphi = \varphi_p$ and its radial and tangential component.

for a part of the arch, ranging from the initial cross-section to the one defined by an arbitrary value of φ.

The particular solutions for the kinematic state variables follow from the Eqs. (12)–(14). Considering homogeneous boundary conditions, the following relations are obtained:

$$
\begin{aligned}
u^L(\varphi) = & \frac{1}{2}\frac{P_r R}{EA}\Big[\sin(\varphi-\varphi_p)-(\varphi-\varphi_p)\cos(\varphi-\varphi_p)\Big]H(\varphi-\varphi_p) \\
& +\frac{1}{2}\frac{P_\varphi R}{EA}\Big[-(\varphi-\varphi_p)\sin(\varphi-\varphi_p)\Big]H(\varphi-\varphi_p) \\
& +\frac{1}{2}\frac{P_r R^3}{EI}\Big[\sin(\varphi-\varphi_p)-(\varphi-\varphi_p)\cos(\varphi-\varphi_p)\Big]H(\varphi-\varphi_p) \\
& +\frac{1}{2}\frac{P_\varphi R^3}{EI}\Big[-(\varphi-\varphi_p)\sin(\varphi-\varphi_p)-2\cos(\varphi-\varphi_p)+2\Big]H(\varphi-\varphi_p),
\end{aligned}
\tag{44}
$$

$$
\begin{aligned}
v^L(\varphi) = & \frac{P_r R}{EA}\Big[\frac{1}{2}(\varphi-\varphi_p)\sin(\varphi-\varphi_p)\Big]H(\varphi-\varphi_p) \\
& +\frac{P_\varphi R}{EA}\Big[-\frac{1}{2}(\varphi-\varphi_p)\cos(\varphi-\varphi_p)-\frac{1}{2}\sin(\varphi-\varphi_p)\Big]H(\varphi-\varphi_p) \\
& +\frac{P_r R^3}{EI}\Big[\frac{1}{2}(\varphi-\varphi_p)\sin(\varphi-\varphi_p)+\cos(\varphi-\varphi_p)-1\Big]H(\varphi-\varphi_p) \\
& +\frac{P_\varphi R^3}{EI}\Big[-\frac{1}{2}(\varphi-\varphi_p)\cos(\varphi-\varphi_p) \\
& +\frac{3}{2}\sin(\varphi-\varphi_p)-(\varphi-\varphi_p)\Big]H(\varphi-\varphi_p),
\end{aligned}
\tag{45}
$$

$$
\begin{aligned}
\theta^L(\varphi) = & \frac{P_r R^2}{EI}\Big[1-\cos(\varphi-\varphi_p)\Big]H(\varphi-\varphi_p) \\
& -\frac{P_\varphi R^2}{EI}\Big[\sin(\varphi-\varphi_p)-(\varphi-\varphi_p)\Big]H(\varphi-\varphi_p).
\end{aligned}
\tag{46}
$$

3.5. Particular solutions for interfacial discontinuities of kinematic variables

Discontinuities of kinematic variables occur at connections between neighboring arch elements, e.g. at hinges or at segment-to-segment interfaces of segmented tunnel rings. They result in rigid body motions. Therefore, the particular solutions for forces and the bending moment vanish, i.e.

$$
N^L(\varphi) = V^L(\varphi) = M^L(\varphi) = 0.
\tag{47}
$$

The rigid body motion, resulting from a discontinuity of the radial displacement, Δu_j, at tangential position φ_j, see Fig. 8(a), can be described by means of the Heaviside function as

$$
u^L(\varphi) = \Delta u_j \cos(\varphi-\varphi_j)H(\varphi-\varphi_j),
\tag{48}
$$
$$
v^L(\varphi) = -\Delta u_j \sin(\varphi-\varphi_j)H(\varphi-\varphi_j),
\tag{49}
$$
$$
\theta^L(\varphi) = 0.
\tag{50}
$$

A discontinuity of the tangential displacement, Δv_j, see Fig. 8(b), yields, analogous to the Eqs. (48)–(50):

$$
u^L(\varphi) = \Delta v_j \sin(\varphi-\varphi_j)H(\varphi-\varphi_j),
\tag{51}
$$
$$
v^L(\varphi) = \Delta v_j \cos(\varphi-\varphi_j)H(\varphi-\varphi_j),
\tag{52}
$$
$$
\theta^L(\varphi) = 0.
\tag{53}
$$

Finally, a discontinuity of the cross-sectional rotation, $\Delta\theta_j$, see Fig. 8(c), yields load integrals reading as

$$
u^L(\varphi) = R\Delta\theta_j \sin(\varphi-\varphi_j)H(\varphi-\varphi_j),
\tag{54}
$$
$$
v^L(\varphi) = -R\Delta\theta_j\Big[1-\cos(\varphi-\varphi_j)\Big]H(\varphi-\varphi_j),
\tag{55}
$$
$$
\theta^L(\varphi) = \Delta\theta_j H(\varphi-\varphi_j).
\tag{56}
$$

3.6. Transfer relations

The load cases considered in the previous subsections are now superimposed. The resulting functions for the static and kinematic variables, i.e. for forces and moment, as well as for displacements and rotation, are arranged in matrix–vector form [36]. The aforementioned variables are collected into a state vector, and a transfer matrix relates the state vector related to the initial cross-section to the state vector characterizing the cross-section at any position φ. Thus,

$$
\begin{bmatrix} u(\varphi) \\ v(\varphi) \\ \theta(\varphi) \\ M(\varphi) \\ N(\varphi) \\ V(\varphi) \\ \hdashline 1 \end{bmatrix} =
\begin{bmatrix}
\cos\varphi & \sin\varphi & T_{13}(\varphi) & T_{14}(\varphi) & T_{15}(\varphi) & T_{16}(\varphi) & \sum u^L(\varphi) \\
-\sin\varphi & \cos\varphi & T_{23}(\varphi) & T_{24}(\varphi) & T_{25}(\varphi) & T_{26}(\varphi) & \sum v^L(\varphi) \\
0 & 0 & 1 & T_{34}(\varphi) & T_{35}(\varphi) & T_{36}(\varphi) & \sum \theta^L(\varphi) \\
0 & 0 & 0 & 1 & T_{45}(\varphi) & T_{46}(\varphi) & \sum M^L(\varphi) \\
0 & 0 & 0 & 0 & \cos\varphi & -\sin\varphi & \sum N^L(\varphi) \\
0 & 0 & 0 & 0 & \sin\varphi & \cos\varphi & \sum V^L(\varphi) \\
\hdashline 0 & 0 & 0 & 0 & 0 & 0 & 1
\end{bmatrix}
\begin{bmatrix} u_i \\ v_i \\ \theta_i \\ M_i \\ N_i \\ V_i \\ \hdashline 1 \end{bmatrix},
\tag{57}
$$

where

$$
T_{13}(\varphi) = R\sin\varphi, \quad T_{14}(\varphi) = \frac{R^2}{EI}(\cos\varphi-1),
$$

$$
T_{15}(\varphi) = \frac{R}{EA}\frac{1}{2}\varphi\sin\varphi + \frac{R^3}{EI}\Big(\frac{1}{2}\varphi\sin\varphi+\cos\varphi-1\Big),
$$

$$
T_{16}(\varphi) = \frac{R}{EA}\Big(\frac{1}{2}\varphi\cos\varphi-\frac{1}{2}\sin\varphi\Big)+\frac{R^3}{EI}\Big(\frac{1}{2}\varphi\cos\varphi-\frac{1}{2}\sin\varphi\Big),
$$

$$
T_{23}(\varphi) = R(\cos\varphi-1), \quad T_{24}(\varphi) = \frac{R^2}{EI}(\varphi-\sin\varphi),
$$

$$
T_{25}(\varphi) = \frac{R}{EA}\Big(\frac{1}{2}\varphi\cos\varphi+\frac{1}{2}\sin\varphi\Big)+\frac{R^3}{EI}\Big(\varphi-\frac{3}{2}\sin\varphi+\frac{1}{2}\varphi\cos\varphi\Big),
$$

$$
T_{26}(\varphi) = \frac{R}{EA}\Big(-\frac{1}{2}\varphi\sin\varphi\Big)+\frac{R^3}{EI}\Big(1-\cos\varphi-\frac{1}{2}\varphi\sin\varphi\Big),
$$

$$
T_{34}(\varphi) = -\frac{R}{EI}\varphi, \quad T_{35}(\varphi) = \frac{R^2}{EI}(\sin\varphi-\varphi), \quad T_{36}(\varphi) = \frac{R^2}{EI}(\cos\varphi-1),
$$

$$
T_{45}(\varphi) = R(1-\cos\varphi), \quad T_{46}(\varphi) = R\sin\varphi.
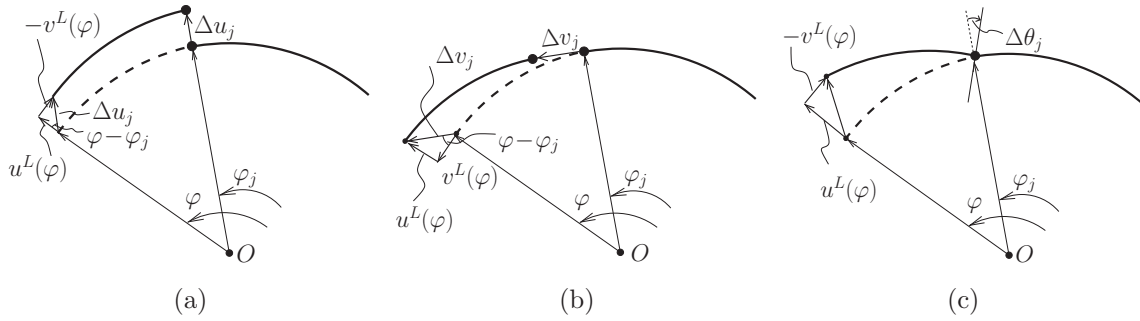\tag{58}
$$

Fig. 8. Interfacial discontinuities of: (a) radial displacement, (b) tangential displacement, and (c) cross-sectional rotation.

The top-left six-by-six submatrix of the transfer matrix in Eq. (57) contains the radius R of the arch, its extensional stiffness EA, and its bending stiffness EI. Load integrals, in turn, form the top six elements of the last column of the transfer matrix. The summation extends over all external loads imposed on the considered arch. This may include integrals for dead load, see Eqs. (27)–(32), point loads, see Eqs. (41)–(46), and interfacial discontinuities of kinematic variables, see Eqs. (47)–(56). The unknown six integration constants form the vector of state variables referring to the initial cross-section of the arch, see u_i, v_i, θ_i, M_i, N_i, and V_i in Eq. (57). They are obtained from the boundary conditions, as will be shown in the following examples.

3.7. Validation example 1: two-hinged arch, subjected to a point load

The two-hinged arch tested by La Poutré [37] is analyzed, see Fig. 9(a). The arch was made of steel and exhibited an I-shaped cross-section, see Fig. 9(b). It is characterized by $EA = 400$ MN and $EI = 0.662272$ MNm^2. A point load was imposed at the crown of the arch. The vertical deflection of the load application point was measured. Under progressively increased loading, the steel started to yield once the point load reached $P_y = 0.059$ MN. The corresponding deflection was equal to $\delta_y = 11.53$ mm.

Structural analysis of the arch focuses on the initial linear elastic behavior. The six integration constants are obtained from the six boundary conditions. Three of them refer to the initial cross-section of the arch. They read as $u_i = v_i = 0$ and $M_i = 0$. They provide direct access to three integration constants. The remaining three integration constants θ_i, N_i, and V_i are identified from the boundary conditions referring to the final cross-section (index "f"). They read as $u_f = v_f = 0$ and $M_f = 0$. To this end, the transfer relations, see Eq. (57), are specified for $\varphi = \pi$ such that the vector on the left-hand side of Eq. (57) contains the state

variables at the final cross-section of the arch. Inserting the corresponding three boundary conditions into this vector delivers the following three algebraic equations for the remaining three integration constants:

$$
\begin{bmatrix} 0 & -2\frac{R^3}{EI} & -\frac{R\pi}{2EA} - \frac{R^3\pi}{2EI} \\ -2R & -\frac{R\pi}{2EA} + \frac{R^3\pi}{2EI} & 2\frac{R^3}{EI} \\ 0 & 2R & 0 \end{bmatrix} \begin{bmatrix} \theta_i \\ N_i \\ V_i \end{bmatrix} = - \begin{bmatrix} \frac{PR}{2EA} + \frac{PR^3}{2EI} \\ \frac{PR\pi}{4EA} + \frac{PR^3}{EI}\left(\frac{\pi}{4} - 1\right) \\ -PR \end{bmatrix}.
$$
(59)

The solution of Eq. (59) reads as:

$$
\theta_i = \frac{PR^4 EA(\pi^2 - 2\pi - 4)}{4\pi\left(EAR^2 + EI\right)EI} + \frac{PR^2(\pi^2 - 2\pi + 4)}{4\pi\left(EAR^2 + EI\right)},
$$
(60)

$$
N_i = \frac{P}{2},
$$
(61)

$$
V_i = -\frac{\left(EAR^2 - EI\right)P}{\left(EAR^2 + EI\right)\pi}.
$$
(62)

The deflection at the crown of the arch is equal to $\delta = -u(\pi/2)$. The latter is obtained by evaluating Eq. (57) for $\varphi = \pi/2$ and inserting the identified integration constants. After simplification, the following result is obtained

$$
\delta = \frac{PR^3}{8EI}(3\pi^2 - 8\pi - 4) + \frac{PR^3(\pi^2 + 12)}{8\pi\left(EAR^2 + EI\right)} + \frac{PREI(\pi^2 - 4)}{8\pi EA\left(EAR^2 + EI\right)}.
$$
(63)

This result is compared with (i) experimental measurements [37], (ii) an available FEM solution [38], and (iii) the solution obtained with the unit force method, see Fig. 10. All three analysis results coincide, provided that the same stiffness of steel is used, see Fig. 10(a). Moreover, the analytical solutions agree very well with the experimental results, provided that the Young's modulus of steel is set equal to 210 GPa, as recommended by Eurocode 3 [39], see Fig. 10(b). This underlines the validity of the presented analytical solution scheme.

3.8. Validation example 2: three-hinged arch under dead load

The considered three-hinged arch is obtained from the analyzed two-hinged arch by inserting a hinge at the crown, see Fig. 11. In the following analysis, the structural behavior under dead load $q = 0.000157$ MN/m is investigated. The transfer relations, see Eq. (57), are specified for the load integrals for dead load, see Eqs. (27)–(32), and for the unknown relative rotation angle at the
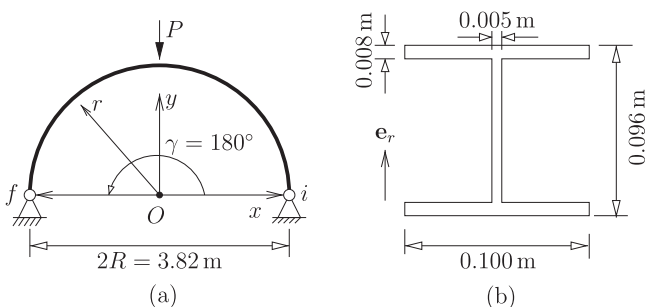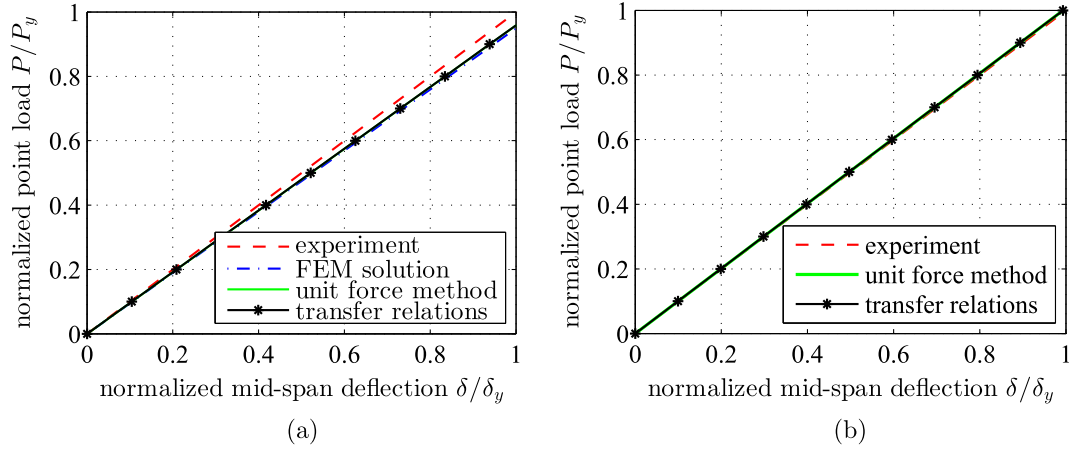

Fig. 9. Two-hinged arch subjected to a point load at its crown: dimensions of (a) the arch and (b) the cross-section.

Fig. 10. Normalized force–deflection diagrams of the two-hinged arch, illustrated in Fig. 9: comparison of experimental data from [37] with the FEM solution from [38] and the analytical solution obtained with the unit force method and the presented transfer relations, see Eq. (63); P_y and δ_y denote the point load and the deflection at the start of yielding of steel: (a) Young's modulus of steel $E_s = 200$ GPa, and (b) Young's modulus of steel $E_s = 210$ GPa.

crown hinge, $\Delta\theta_h$, see Eqs. (47) and (54)–(56). The seven unknowns, i.e. the six integration constants and the unknown relative rotation angle $\Delta\theta_h$, are obtained from six boundary conditions $u_i = v_i = 0$, $M_i = 0$ and $u_f = v_f = 0$, $M_f = 0$ and from the transition condition $M_h = 0$ at the crown hinge. The integration constants at the initial cross-section provide direct access to three integration constants. The following four algebraic equations are then obtained for θ_i, N_i, V_i, and $\Delta\theta_h$:

$$\begin{bmatrix} 0 & -2\frac{R^3}{EI} & -\frac{R\pi}{2EA} - \frac{R^3\pi}{2EI} & R \\ -2R & -\frac{R\pi}{2EA} + \frac{R^3\pi}{2EI} & 2\frac{R^3}{EI} & -R \\ 0 & 2R & 0 & 0 \\ 0 & R & R & 0 \end{bmatrix} \begin{bmatrix} \theta_i \\ N_i \\ V_i \\ \Delta\theta_h \end{bmatrix} = \begin{bmatrix} \frac{\pi R^2 q}{4EA} + \frac{3\pi R^4 q}{4EI} \\ \frac{\pi^2 R^2 q}{4EA} - \frac{R^4 q}{EI}\left(4 - \frac{\pi^2}{4}\right) \\ -\pi R^2 q \\ -R^2 q \end{bmatrix}.$$

(64)

The solution of Eq. (64) reads as

$$\theta_i = \frac{qR^3}{8EI}\left(-3\pi^2 + 7\pi + 8\right) + \frac{qR}{8EA}\left(-\pi^2 + \pi\right),$$

(65)

$$N_i = -\frac{1}{2}\pi q R,$$

(66)

$$V_i = \frac{1}{2}qR(\pi - 2),$$

(67)

$$\Delta\theta_h = \frac{qR^3}{4EI}\left(\pi^2 - 3\pi\right) + \frac{qR}{4EA}\left(\pi^2 - \pi\right).$$

(68)

Based on the obtained integration constants and the relative rotation angle, the state vector at an arbitrary cross-section of interest can be determined by evaluating the transfer relations, see Eq. (57), for the respective polar angle φ. The displacement components u and v follow from the first two lines of the transfer relations, reading as

$$u(\varphi) = \frac{qR^4}{8EI}\left[(2\varphi^2 - 2\pi\varphi - 3\pi^2 + 5\pi + 6)\sin\varphi + 2(\pi\varphi + \varphi - 2\pi)\cos\varphi + 4\pi\right]$$
$$+ \frac{qR^2}{8EA}\left[(2\varphi^2 - 2\pi\varphi - \pi^2 - \pi + 2)\sin\varphi + 2\varphi(\pi - 1)\cos\varphi\right]$$
$$- \left[\frac{\pi q R^4}{4EI}(\pi - 3) + \frac{\pi q R^2}{4EA}(\pi - 1)\right]H\left(\varphi - \frac{\pi}{2}\right)\cos\varphi,$$

(69)

$$v(\varphi) = \frac{qR^4}{8EI}\left[2(3\pi - \pi\varphi - 3\varphi)\sin\varphi + (2\varphi^2 - 2\pi\varphi - 3\pi^2 + 3\pi)\cos\varphi - 4\pi\varphi + 3\pi^2\right.$$
$$\left. - 3\pi\right] + \frac{qR^2}{8EA}\left[2(3\varphi - \pi\varphi - \pi)\sin\varphi + (2\varphi^2 - 2\pi\varphi - \pi^2 + \pi)\cos\varphi + \pi^2 - \pi\right]$$
$$- \left[\frac{\pi q R^4}{4EI}(\pi - 3) + \frac{\pi q R^2}{4EA}(\pi - 1)\right]H\left(\varphi - \frac{\pi}{2}\right)(1 - \sin\varphi).$$

(70)
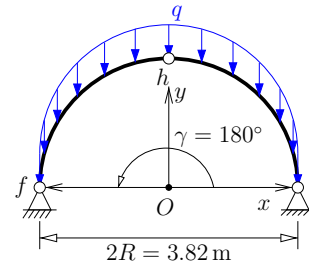
Fig. 11. Three-hinged arch subjected to dead load $q = 0.000157$ MN/m.
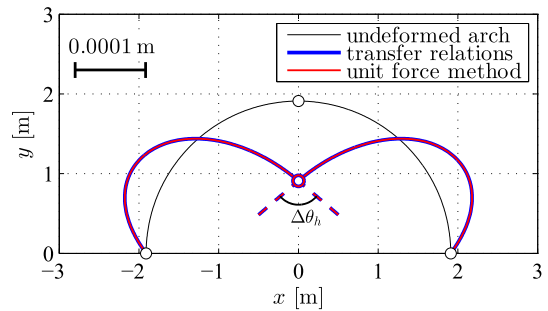
Fig. 12. Comparison of the deformed configuration of the three-hinged arch, see Fig. 11, obtained by the transfer relations, see Eqs. (69) and (70), and by the unit force method, see Appendix B.

They provide access to the deformed configuration of the arch, see also Fig. 12. In order to check the validity of Eqs. (69) and (70), the unit force method is used to calculate the horizontal and the vertical displacement component at an arbitrary point of the arch, see Appendix B. The two independently derived analytical results coincide, see Fig. 12. This underlines the validity of the transfer relations, the load integrals for dead load, and the load integrals for relative rotation angles.

4. Hybrid analysis of the segmented tunnel ring

The tangential coordinate φ is measured from the crown of the segmented tunnel ring (Fig. 2), i.e. from the cross-section

in the middle of segment K. The structure is analyzed by means of *one* transfer matrix, containing 42 sets of known load integrals: 24 of them are related to point loads and 18 to three displacement/rotation discontinuities each at the six interfaces between neighboring segments (Fig. 3). The ring was tested on a lab floor (Fig. 1). Therefore, gravity forces were acting in the axial direction and, thus, did not interfere with the structural analysis.

The only unknowns involved in the transfer relations are the six integration constants, representing the six state variables at the crown. They are identified as follows. Noting that a closed ring is statically indeterminate to the third degree, three geometric continuity conditions are required for determination of the forces and the bending moment at the crown. To this end, the transfer relations, see Eq. (57), are specified for $\varphi = 2\pi$, in order to provide a relation between the state variables at the initial (index "i") and the final (index "f") cross-section. Noting that the initial cross-section is *equal* to the final cross-section, the geometrical compatibility conditions read as $u_f = u_i$, $v_f = v_i$, and $\theta_f = \theta_i$. They allow for determination of the internal forces at the crown, i.e. of M_i, N_i, and V_i. This is done numerically. Based on the units of measurement "Meganewton", "Megapascal",

and "Meter", the condition number of the system matrix is equal to 43. This indicates reliable numerical solutions, see Table 1. The remaining integration constants, i.e. the kinematic state variables at the crown, u_i, v_i, and θ_i, may be set equal to small arbitrary values, because they refer to rigid body motions. The latter do not influence the predicted relative displacement convergences.

Based on the obtained integration constants, the transfer relations allow for computing all six state variables at any position of interest by means of a simple matrix-vector product, see Eq. (57). This enables computation of deformed configurations, as well as of the distributions of the internal forces and of the normal stresses, see Eq. (8) as well as Figs. 13 and 14.

The ring structure responds unsymmetrically to the symmetric external loads, see the deformed configurations, illustrated in Fig. 13. The unsymmetric response is also clearly visible in the bending moment distributions. The first load increment activates the largest bending moments in the crown region, see Fig. 14(a). At the second load increment, significant bending moments develop also in the lateral parts and in the bottom region, see Fig. 14(d). The third load increment results in bending moments mainly in the left lateral part of the segmented ring, see Fig. 14

Table 1
Numerical values of the point loads and of the internal forces at the crown.

Load step	P_1 [MN]	P_2 [MN]	P_3 [MN]	M_i [MNm]	N_i [MN]	V_i [MN]
1	0.02550	0.01514	0.01519	−0.03567	−0.05604	0.01181
2	0.05543	0.03442	0.04124	−0.05170	−0.14271	0.02689
3	0.08535	0.05370	0.06729	−0.07160	−0.22701	0.04753
4	0.11727	0.07105	0.09134	−0.08887	−0.30893	0.06491
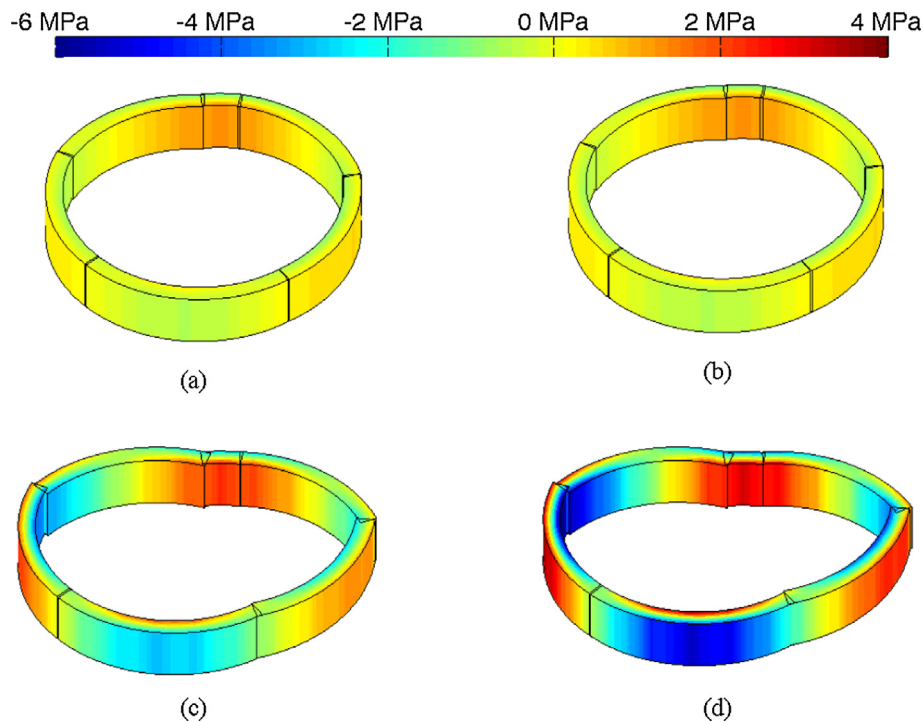
Fig. 13. Deformed configuration of the analyzed segmented tunnel ring and distribution of the normal stresses according to Eq. (8), see also the bending moments and normal forces in Fig. 14: (a) load step 1, (b) load step 2, (c) load step 3, and (d) load step 4; the magnification factor of the displacements amounts to 50.
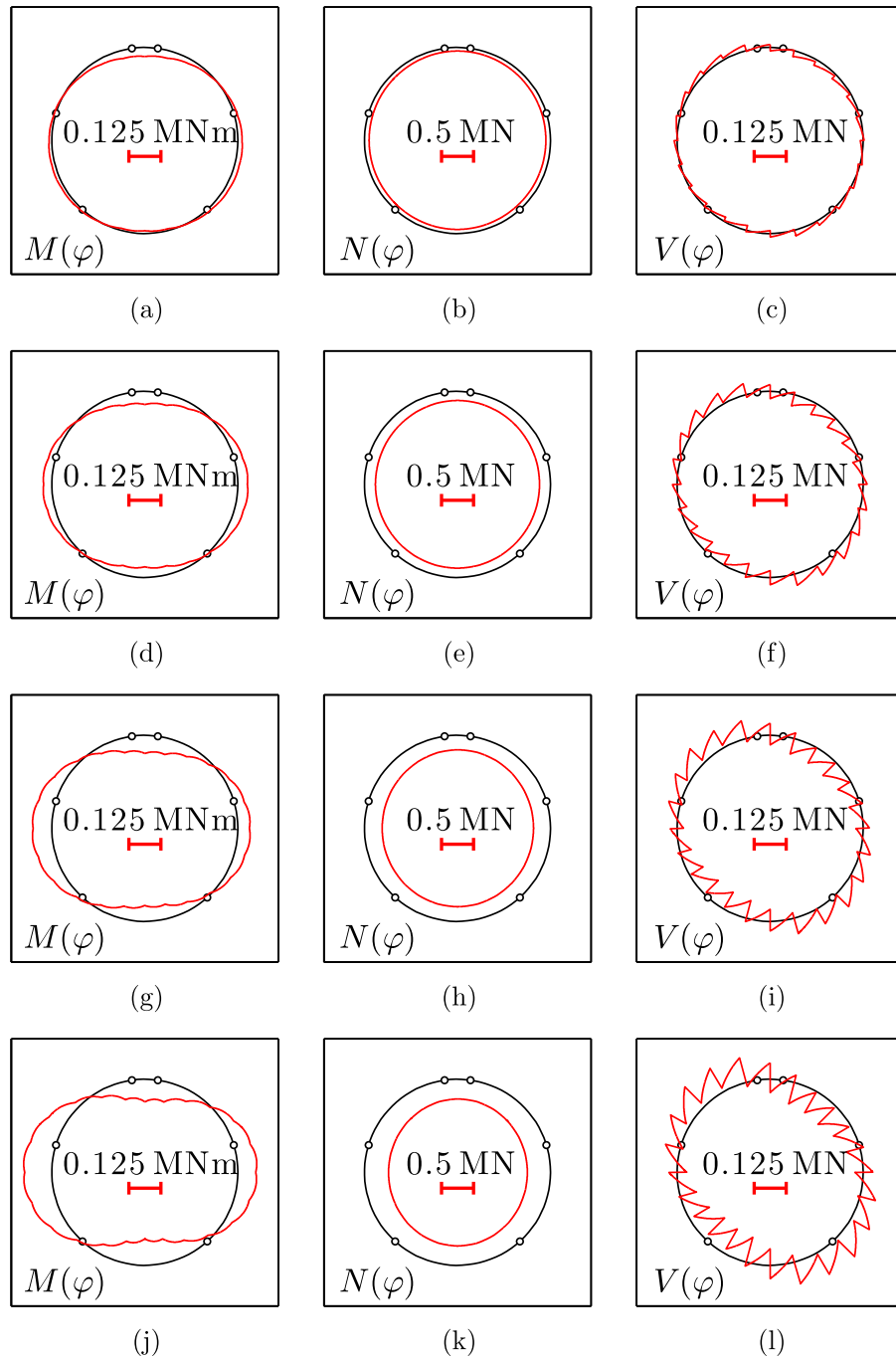
Fig. 14. Distributions of internal forces of the analyzed segmented tunnel ring: (a) – (c) load step 1, (d) – (f) load step 2, (g) – (i) load step 3, and (j) – (l) load step 4; the small circles illustrate positions of segment-to-segment interfaces.

(g). The final load increment, in turn, yields an increase of the bending moments particularly in the right lateral part and in the bottom region, see Fig. 14(j).

Non-smoothness due to the point loads occurs in the bending moment distributions, see the kinks in Fig. 14(a), (d), (g), and (j), whereas discontinuities occur in the shear force distributions, see the jumps in Fig. 14(c), (f), (i), and (l). The normal force distributions, however, remain relatively smooth throughout the test, see Fig. 14(b), (e), (h), and (k).

The maximum tensile normal stress occurs at load step 4 on the inner surface of the bottom segment *C*. It amounts to 3.56 MPa.

Since this is close to the tensile strength of the concrete, load step 4 refers to the elastic limit of the investigated structure. This is consistent with experimental observations [1].

In order to further check the reliability of the presented results, model-predicted convergences are computed. They agree well with the measured convergences, as quantified by the quadratic correlation coefficient amounting to $r^2 = 0.9995$, see also Fig. 15. Notably, this comparison is a nontrivial assessment of the predictive capabilities of the transfer relations, since the convergences are independent of the point loads and interfacial discontinuities.
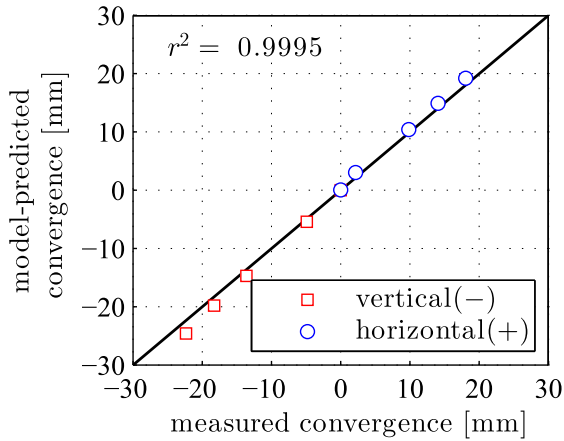
Fig. 15. Comparison of model-predicted and experimentally measured convergences.

5. Discussion

The following discussion refers to (i) the reason for the unsymmetric structural response under symmetric external loading, (ii) the question whether the tested segmented tunnel ring may be treated as a slender arch, and (iii) the benefits from the presented hybrid approach.

5.1. Initial geometric imperfections as the reason for the unsymmetric structural response

In order to explain the unsymmetric structural behavior, two load cases are considered. Load case (I) accounts for the point loads. However, all interfacial discontinuities are set equal to zero. Load case (II) considers all of the interfacial discontinuities. However, all point loads are set equal to zero. Load case (I) results in symmetric distributions of the bending moments and the normal forces and in an antisymmetric distribution of the shear forces, see Fig. 16.
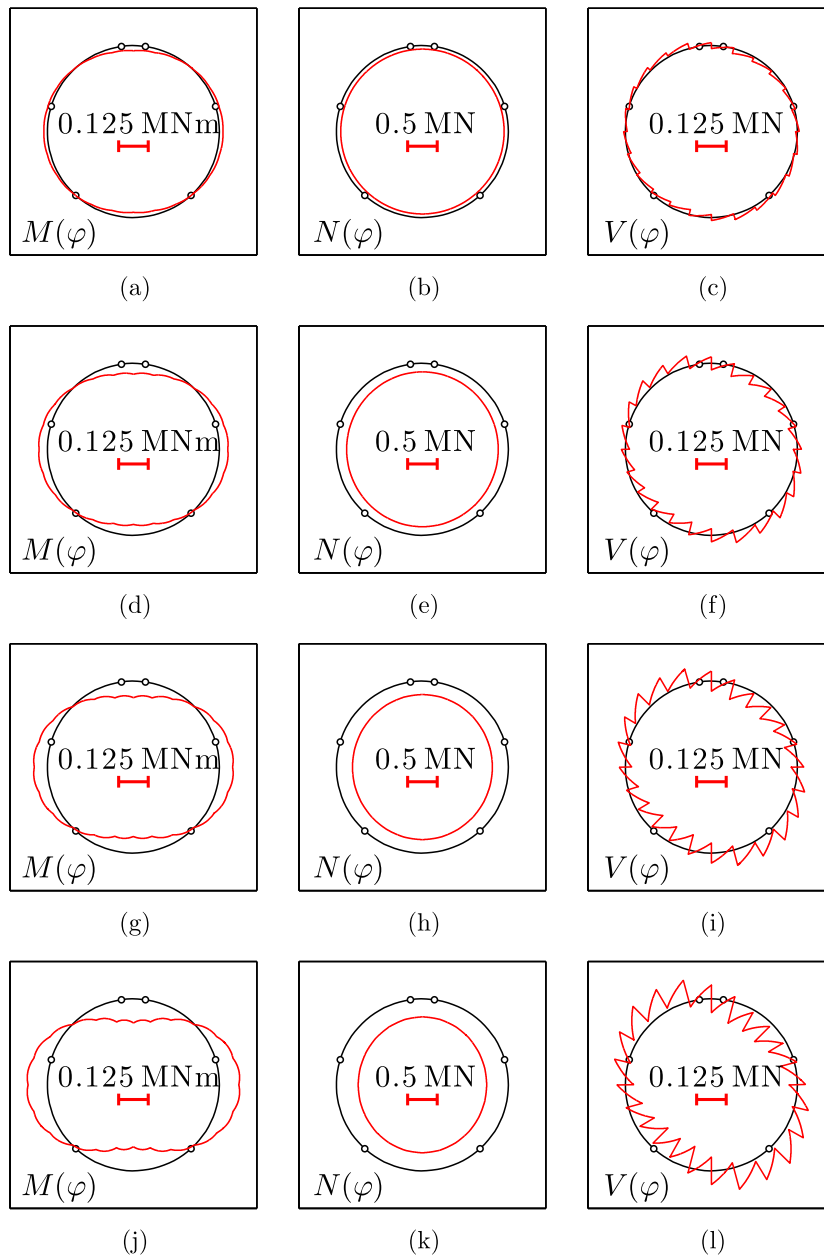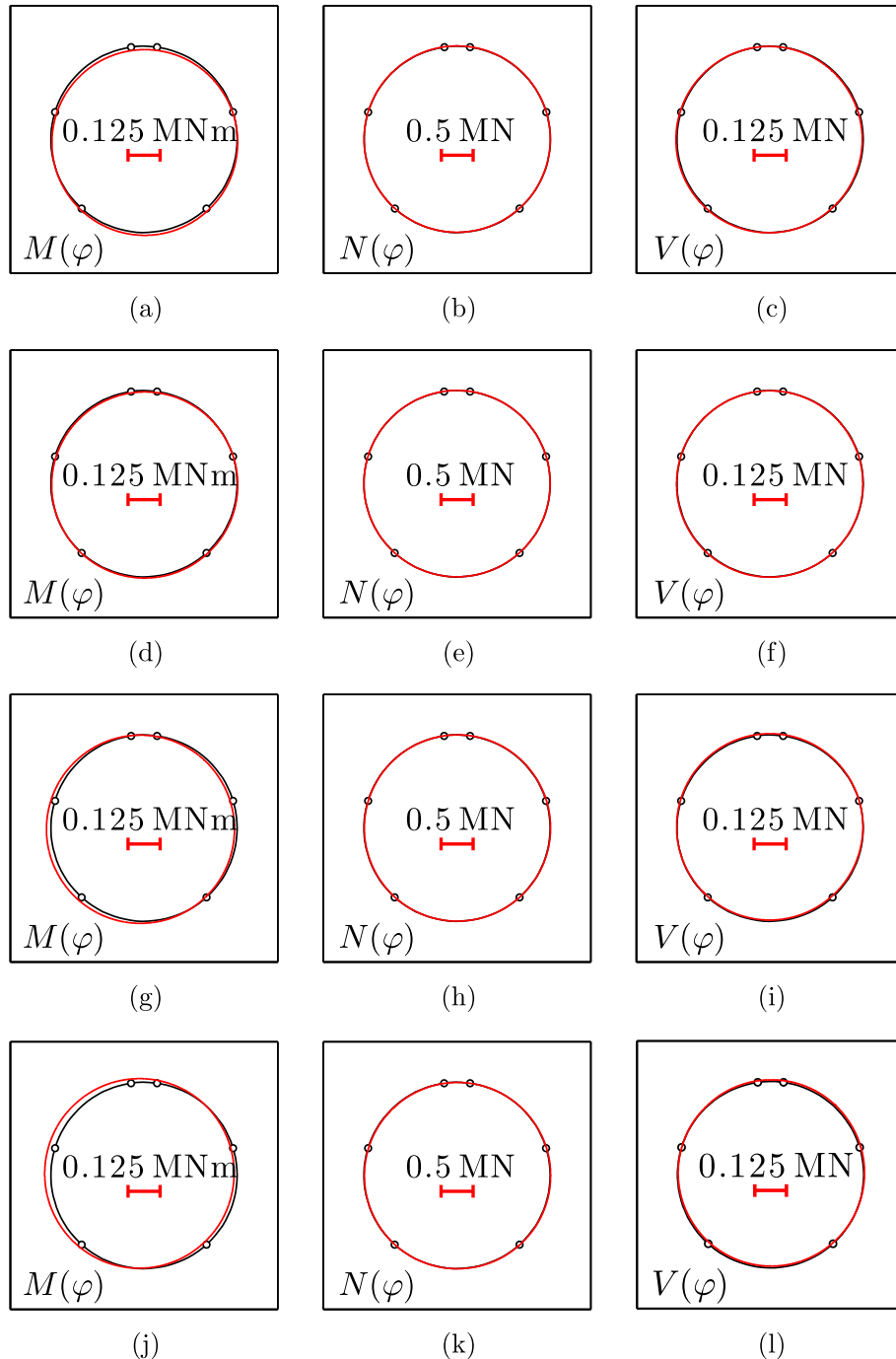

Fig. 16. Distributions of internal forces of the analyzed segmented tunnel ring, considering points loads only and setting the interfacial discontinuities equal to zero: (a) – (c) load step 1, (d) – (f) load step 2, (g) – (i) load step 3, and (j) – (l) load step 4.

Notably, the magnitudes of the internal forces are very similar to the ones obtained in the full structural analysis, compare Fig. 16 with Fig. 14. Load case (II), in turn, results in unsymmetric distributions of the internal forces, see Fig. 17. Remarkably, the magnitudes of the internal forces are very small compared to load case (I). This underlines the fact that the measured interfacial discontinuities primarily result in rigid body motions of the segments. This suggests (i) that the initial configuration – albeit being close to a perfect ring – exhibited small geometric imperfections (amounting to a few millimeters), and (ii) that rigid body motions of the segments removed or, at least, reduced these imperfections in the analyzed load steps, such that the tunnel ring exhibited an almost symmetric configuration at later stages of the test [1]. This also clarifies that

the measured discontinuities of the tangential displacements refer to establishing full-face contact in the interfacial contact regions, starting from an initially imperfect contact. They do not refer to overlapping of neighboring tunnel segments and, thus, not to crushing of concrete, which would be preceded by very large compressive normal forces.

5.2. Does the tested ring qualify for the analysis as a slender arch?

The slenderness is defined as H/R. In the given case, $H/R = 35/292.5 \approx 0.12$ which is relatively small, but not very small compared to 1. This renders the slenderness assumption $R/r \approx 1$ questionable, see, e.g. [40]. Notably, the slenderness

Fig. 17. Distributions of internal forces of the analyzed segmented tunnel ring, considering interfacial discontinuities only and setting the point loads equal to zero: (a) – (c) load step 1, (d) – (f) load step 2, (g) – (i) load step 3, and (j) – (l) load step 4.

assumption was used for the derivation of the constitutive Eqs. (3) and (4) and of the expression for the normal stresses as a function of the normal force and the bending moment, see Eq. (8). In order to clarify whether or not the tested ring qualifies for the analysis as a slender arch, the structural analysis is repeated for $R/r \not\approx 1$. This results in constitutive relations containing couplings (i) of the normal force and the change of curvature of the axis of the arch, and (ii) of the bending moment and the normal strain of the axis of the arch:

$$N = \widehat{EA}\left(\frac{u}{R} + \frac{1}{R}\frac{dv}{d\varphi}\right) + \widehat{EK}\left(\frac{1}{R^2}\frac{d^2u}{d\varphi^2} + \frac{1}{R^2}\frac{dv}{d\varphi}\right), \tag{71}$$

$$M = \widehat{EK}\left(\frac{u}{R} + \frac{1}{R}\frac{dv}{d\varphi}\right) + \widehat{EI}\left(\frac{1}{R^2}\frac{d^2u}{d\varphi^2} + \frac{1}{R^2}\frac{dv}{d\varphi}\right). \tag{72}$$

In addition, the following expression for the normal stresses as a function of the normal force and the bending moment is obtained:

$$\sigma_{\varphi\varphi} = E\left[\frac{N\widehat{EI} - M\widehat{EK}}{\widehat{EA}\widehat{EI} - \widehat{EK}^2} - (r - R)\frac{N\widehat{EK} - M\widehat{EA}}{\widehat{EA}\widehat{EI} - \widehat{EK}^2}\right]\frac{R}{r}. \tag{73}$$

Table 2
Numerical values of $EA, EI, \widehat{EA}, \widehat{EI},$ and $\widehat{EK}$, for the investigated segmented tunnel ring.

$R/r \approx 1$	$R/r \not\approx 1$
EA = 18,620 MN	$\widehat{EA}$ = 18,282 MN
EI = 186 MNm²	$\widehat{EI}$ = 187 MNm²
	$\widehat{EK}$ = −64 MNm

Notably, Eq. (73) describes a *nonlinear* distribution of the normal stresses across the thickness of tunnel segments.

In Eqs. (71)–(73), $\widehat{EA}$, $\widehat{EI}$, and $\widehat{EK}$ stand for the geometrically enriched extensional and bending stiffnesses, and for a coupling stiffness, respectively. They read as

$$\widehat{EA} = \int_A E\,\frac{R}{r}\,dA, \tag{74}$$

$$\widehat{EK} = \int_A E\,\frac{R}{r}(r - R)\,dA, \tag{75}$$

$$\widehat{EI} = \int_A E\,\frac{R}{r}(r - R)^2\,dA. \tag{76}$$

For the investigated tunnel ring, the values for $\widehat{EA}$ and $\widehat{EI}$ differ by only a few percent from the ones for EA and EI, see Table 2.

Since the geometrically enriched constitutive Eqs. (71) and (72) are more complicated than their counterparts given in Eqs. (3) and (4), the strategy for solving the differential equations for u and v needs to be modified as well. In this context, Eqs. (12) and (13) need to be replaced by

$$\frac{d^2u}{d\varphi^2} + u = N\frac{\widehat{EI}R + \widehat{EK}R^2}{\widehat{EI}\widehat{EA} - \widehat{EK}^2} - M\frac{\widehat{EK}R + \widehat{EA}R^2}{\widehat{EI}\widehat{EA} - \widehat{EK}^2}, \tag{77}$$

$$\frac{dv}{d\varphi} = N\frac{\widehat{EI}R}{\widehat{EA}\widehat{EI} - \widehat{EK}^2} - M\frac{\widehat{EK}R}{\widehat{EA}\widehat{EI} - \widehat{EK}^2} - u. \tag{78}$$

Thus, the analytical solutions for the kinematic variables are more complicated than those presented in Section 3, provided that $R/r \not\approx 1$ is considered. Still, the geometrically enriched transfer relations can be derived by analogy to the procedure described in
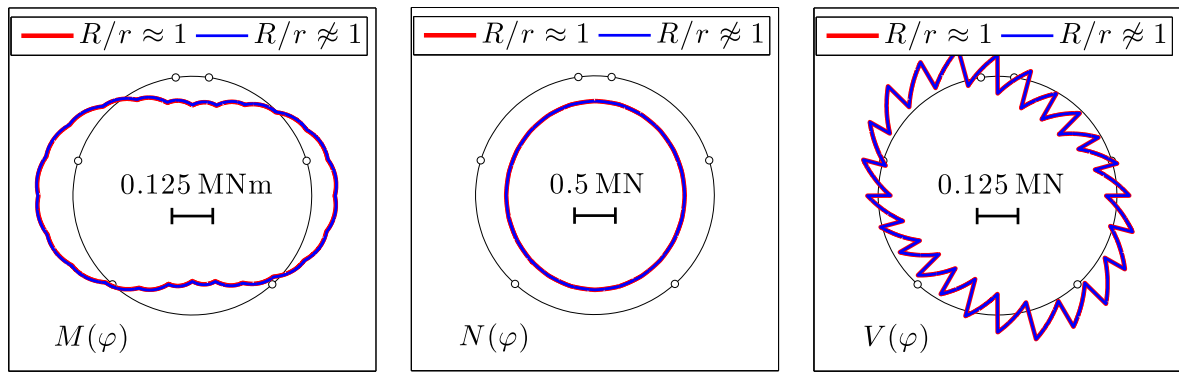
Fig. 18. Comparison of internal force distributions at load step 4, considering the slenderness assumption $R/r \approx 1$, see the red graphs, and $R/r \not\approx 1$, see the blue graphs: (a) bending moments, (b) normal forces, (c) shear forces.
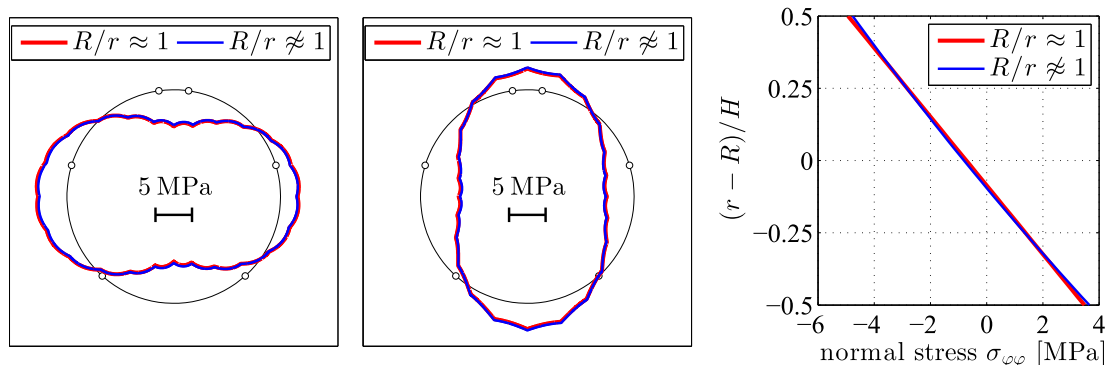
Fig. 19. Comparison of the normal stress distributions at load step 4, considering $R/r \approx 1$, see the red graphs, and $R/r \not\approx 1$, see the blue graphs: normal stresses at (a) the outer surface and (b) the inner surface; (c) normal stress distribution along the thickness of the middle cross-section of segment C.

Section 3. In the following, they are used for the structural analysis of the tunnel ring, as described in Section 4.

The solutions obtained for $R/r \not\approx 1$ and for the slenderness assumption $R/r \approx 1$ are virtually the same. The maximum difference regarding the internal forces at load step 4 amounts to only 1.2%, see Fig. 18. The maximum differences regarding the normal stresses at the inner and the outer surface of the segments are less than 3.5%, see Fig. 19. In addition, the nonlinear normal stress distributions, described by Eq. (73), are close to the linear distributions described by Eq. (8), see Fig. 19(c). This underlines that the analyzed tunnel ring indeed qualifies for the analysis by means of the transfer relations based on the slenderness assumption $R/r \approx 1$.

5.3. Benefits from the hybrid approach

The presented hybrid approach uses *prescribed* point loads and *measured* interfacial discontinuities of displacements/rotations as input. This is different from the standard approach which (i) uses only the prescribed loading as input and (ii) requires a mathematical model for the structural behavior of segment-to-segment interfaces [20–25]. The mechanical behavior at these interfaces is nonlinear due to phenomena such as interfacial separation, frictional sliding, diffuse cracking, and crushing of concrete. Corresponding nonlinear interface models require an iterative solution strategy even if the segments behave in a linear elastic fashion. The proposed hybrid formulation, on the other hand, uses measured interfacial discontinuities as input. This eliminates the interfacial nonlinearities and, thus, simplifies the structural analysis significantly.

6. Conclusions

The presented hybrid method for segmented tunnel rings contains transfer relations, representing analytical solutions of the basic equations of first-order theory for slender circular arches with constant cross-sectional properties. As for these transfer relations, the following conclusion is drawn:

- As highlighted in the two validation examples, the transfer relations allow for deriving analytical solutions for many arch problems of interest. This requires only the formulation of boundary and transition conditions, as well as the corresponding solution of linear algebraic systems of equations. Thereafter, the transfer relations provide analytical functions for all six state variables of interest: the radial and tangential displacement, the cross-sectional rotation angle, the bending moment, and the normal and shear force. This renders the transfer relations an attractive topic in classes on "Structural Analysis".

As for the developed hybrid method and for its application to the segmented tunnel ring, the following conclusions are drawn:

- The developed transfer relations are very valuable for hybrid analysis of a displacement-monitored segmented tunnel ring, because the whole ring, consisting of *six* segments, can be analyzed with *one* transfer matrix, containing 24 sets of known load integrals for the imposed point loads and 18 sets of known load integrals for the *measured* discontinuities of the three kinematic variables at the six segment-to-segment interfaces. This way, the hybrid analysis of each load step essentially requires the solution of an algebraic system of only three equations, referring to the continuity of displacements and of the cross-sectional rotation at the crown of the ring. Thereafter, the transfer relations provide *analytical* solutions for all six

variables of interest: N, V, M, u, v, and θ. These solutions can be simply *evaluated* for any position φ of interest. Therefore, the transfer relations are computationally very efficient.

- There is no need to explicitly model the nontrivial behavior of segment-to-segment interfaces in the developed hybrid method. This is possible because it uses imposed point loads and measured interfacial discontinuities as input. This is different from more classical approaches to the same problem, see [41]. Therein, a nonlinear interface model required incremental-iterative solution schemes even for linear elastic behavior of the reinforced concrete segments.

- The developed hybrid analysis provides valuable insight into the load-carrying behavior of displacement-monitored segmented tunnel rings. The performed hybrid analysis underlines that very small imperfections of the initial assembly of segmented tunnel rings may lead to a remarkably unsymmetric structural behavior.

As for future work, it is planned to extend the developed hybrid method towards consideration of inelastic material behavior, such as tensile cracking of concrete and yielding of the steel reinforcements.

Appendix A. Small strain ("first-order") theory for slender circular arches

The tool for the development of this basically well-known theory is the principle of virtual power. Its involvement is motivated by the possibility of a mechanically consistent derivation of relations, some of which have been used for a long time without analyzing their scientific background. The principle of virtual power [42–45] is particularly useful for the transition from three-dimensional continuum mechanics to the presently considered arch theory. It reads as

$$\mathcal{P}^{ext} + \mathcal{P}^{int} = 0, \tag{A.1}$$

with

$$\mathcal{P}^{ext} = \int_V \mathbf{f}(r,\varphi,z) \cdot \dot{\mathbf{u}}(r,\varphi,z;t)dV + \int_{\partial V} \mathbf{T}(\mathbf{n};r,\varphi,z) \cdot \dot{\mathbf{u}}(r,\varphi,z;t)\ dA, \tag{A.2}$$

$$\mathcal{P}^{int} = -\int_V \boldsymbol{\sigma} : \dot{\mathbf{d}}\ dV, \tag{A.3}$$

where $\mathcal{P}^{ext}$ and $\mathcal{P}^{int}$ denote the virtual power of the external forces and of the internal forces, respectively, $\mathbf{f}(r,\varphi,z)$ stands for volume forces, $\mathbf{T}(\mathbf{n};r,\varphi,z)$ denotes the surface tractions with $\mathbf{n}$ as the unit surface normal vector; $\dot{\mathbf{u}}(r,\varphi,z;t)$ stands for the virtual velocity field, $\boldsymbol{\sigma}$ for the real stress field, and $\dot{\mathbf{d}}$ for the Eulerian strain rate tensor.

The radius of curvature of slender circular arches, R, is significantly larger than the cross-sectional dimensions. The latter are considered to be constant along the axis of the arch. The position of an arbitrary point of the arch is described by a cylindrical coordinate system, with the base vectors $\mathbf{e}_r$, $\mathbf{e}_\varphi$, and $\mathbf{e}_z$ (Fig. A.1).
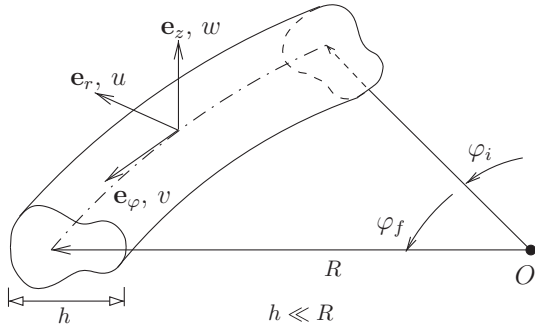
Fig. A.1. Circular arch of radius R in the undeformed configuration: illustration of the base vectors $\mathbf{e}_r$, $\mathbf{e}_\varphi$, and $\mathbf{e}_z$; the values φ_i and φ_f of φ refer to the initial and the final cross-section of the arch.

A.1. Kinematic description

The displacement field of an arch is given by the Eqs. (1) and (2). The underlying kinematic assumptions read as follows:

1. Arches are loaded in the r, φ - plane.
2. Each cross-section performs a *rigid body motion*.
3. Cross-sectional rotations are *small*, such that the circular paths of the cross-sectional points can be approximated by the initial tangents to these paths.
4. All cross-sections remain, at any time, *orthogonal* to the axis of the arch.
5. The displacements are small compared with the cross-sectional dimensions. This allows to refer the analysis to the coordinates that describe the undeformed system.

In cylinder coordinates, the vanishing components of the linearized strain tensor read as $\varepsilon_{rr} = \varepsilon_{zz} = \varepsilon_{\varphi r} = \varepsilon_{\varphi z} = \varepsilon_{zr} = 0$. The only non-vanishing component is the normal strain in the tangential direction

$$\varepsilon_{\varphi\varphi}(r,\varphi,z) = \frac{u(\varphi)}{r} + \frac{1}{r}\frac{dv(\varphi)}{d\varphi}$$
$$- \frac{r-R}{r}\left(\frac{1}{R}\frac{d^2 u(\varphi)}{d\varphi^2} - \frac{1}{R}\frac{dv(\varphi)}{d\varphi}\right). \quad \text{(A.4)}$$

A.2. Virtual power of the external forces: stress resultants

The virtual power of the external forces involves volume forces $\mathbf{f}(r,\varphi,z)$ and surface tractions $\mathbf{T}(r,\varphi,z)$:

$$\mathbf{f}(r,\varphi,z) = f_r(r,\varphi,z)\mathbf{e}_r(\varphi) + f_\varphi(r,\varphi,z)\mathbf{e}_\varphi(\varphi) + f_z(r,\varphi,z)\mathbf{e}_z, \quad \text{(A.5)}$$

$$\mathbf{T}(\mathbf{n};r,\varphi,z) = T_r(r,\varphi,z)\mathbf{e}_r(\varphi) + T_\varphi(r,\varphi,z)\mathbf{e}_\varphi(\varphi) + T_z(r,\varphi,z)\mathbf{e}_z. \quad \text{(A.6)}$$

They produce power along the virtual velocity field, which is described analogous to the real displacements, see Eq. (1), as

$$\dot{\mathbf{u}}(r,\varphi,z;t) = \dot{u}(\varphi;t)\mathbf{e}_r$$
$$+ \left[\dot{v}(\varphi;t) - (r-R)\left(\frac{1}{R}\frac{\partial\dot{u}(\varphi;t)}{\partial\varphi} - \frac{\dot{v}(\varphi;t)}{R}\right)\right]\mathbf{e}_\varphi. \quad \text{(A.7)}$$

Determination of the virtual power of the external forces, see Eq. (A.2), produced by tractions, see Eq. (A.6), and by body forces, see Eq. (A.5), along the virtual velocities, see Eq. (A.7), includes stress resultants which are energetically conjugate to the three degrees of freedom of the cross-section of the arch, namely to give the mathematical symbols of the degree of freedom: line loads $q_r(\varphi)$ and $q_\varphi(\varphi)$, distributed moments $m(\varphi)$, normal forces $N(\varphi)$, shear forces $V(\varphi)$, and bending moments $M(\varphi)$, see Fig. A.2. Thus, the virtual power of the external forces reads as

$$\mathcal{P}^{ext} = \int_{\varphi_i}^{\varphi_f} q_r(\varphi)\,\dot{u}(\varphi;t)\,R\,d\varphi + \int_{\varphi_i}^{\varphi_f} q_\varphi(\varphi)\,\dot{v}(\varphi;t)\,R\,d\varphi$$
$$- \int_{\varphi_i}^{\varphi_f} m(\varphi)\left(\frac{1}{R}\frac{\partial\dot{u}(\varphi;t)}{\partial\varphi} - \frac{\dot{v}(\varphi;t)}{R}\right)R\,d\varphi + N(\varphi)\,\dot{v}(\varphi;t)\Big|_{\varphi_i}^{\varphi_f}$$
$$- M(\varphi)\left(\frac{1}{R}\frac{\partial\dot{u}(\varphi;t)}{\partial\varphi} - \frac{\dot{v}(\varphi;t)}{R}\right)\Big|_{\varphi_i}^{\varphi_f} + V(\varphi)\,\dot{u}(\varphi;t)\Big|_{\varphi_i}^{\varphi_f}, \quad \text{(A.8)}$$

with

$$q_r(\varphi) = \int_A f_r(r,\varphi,z)\,\frac{r}{R}\,dA + \int_C T_r(\mathbf{n}_s;r,\varphi,z)\,\frac{r}{R}\,ds, \quad \text{(A.9)}$$

$$q_\varphi(\varphi) = \int_A f_\varphi(r,\varphi,z)\,\frac{r}{R}\,dA + \int_C T_\varphi(\mathbf{n}_s;r,\varphi,z)\,\frac{r}{R}\,ds, \quad \text{(A.10)}$$

$$m(\varphi) = \int_A f_\varphi(r,\varphi,z)(r-R)\,\frac{r}{R}\,dA + \int_C T_\varphi(\mathbf{n}_s;r,\varphi,z)(r-R)\,\frac{r}{R}\,ds, \quad \text{(A.11)}$$

$$N(\varphi) = \int_A \sigma_{\varphi\varphi}(r,\varphi,z)\,dA, \quad \text{(A.12)}$$

$$V(\varphi) = \int_A \sigma_{\varphi r}(r,\varphi,z)\,dA, \quad \text{(A.13)}$$

$$M(\varphi) = \int_A \sigma_{\varphi\varphi}(r,\varphi,z)(r-R)\,dA. \quad \text{(A.14)}$$

where C denotes the cross-sectional contour of the arch, s is the arc-length measured along the contour, and $\mathbf{n}_s$ is the unit surface normal vector at s. The stress resultants of Eqs. (A.12)–(A.14), only contain normal stresses $\sigma_{\varphi\varphi}$ and shear stresses $\sigma_{\varphi r}$, underlining that
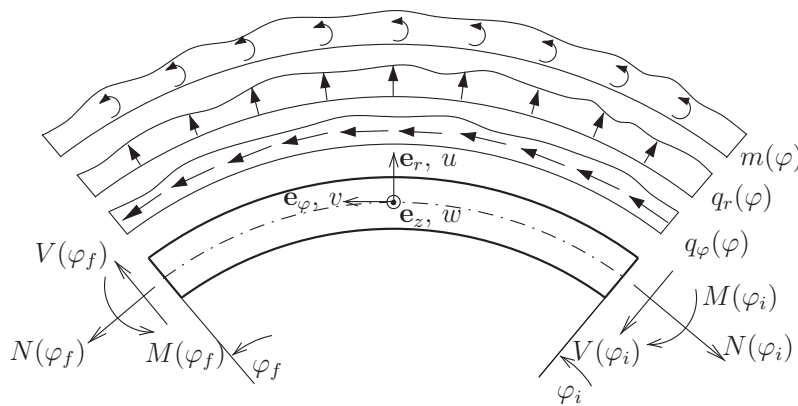
Fig. A.2. Positive line loads $q_\varphi(\varphi)$ and $q_r(\varphi)$ and positive line moments $m(\varphi)$, acting in the direction of the local base vectors $\mathbf{e}_r$, $\mathbf{e}_\varphi$, $\mathbf{e}_z$.

stress states in slender arches are governed by $\sigma_{\varphi\varphi}$ and $\sigma_{\varphi r}$. All other independent stress components may be disregarded.

A.3. Constitutive relations

Normal stresses $\sigma_{\varphi\varphi}$ appearing in the definitions of the normal forces $N(\varphi)$ and the bending moments $M(\varphi)$, see Eqs. (A.12) and (A.14), can be related to normal strain, via Hooke's law:

$$\sigma_{\varphi\varphi}(r, \varphi, z) = E\varepsilon_{\varphi\varphi}(r, \varphi, z), \tag{A.15}$$

where E denotes Young's modulus. Substitution of Eq. (A.4) into Eq. (A.15), and insertion of the result into Eqs. (A.12) and (A.14), gives

$$N(\varphi) = \int_A E\left[\frac{u(\varphi)}{r} + \frac{1}{r}\frac{dv(\varphi)}{d\varphi} - \frac{r-R}{r}\left(\frac{1}{R}\frac{d^2u(\varphi)}{d\varphi^2} - \frac{1}{R}\frac{dv(\varphi)}{d\varphi}\right)\right] dA \tag{A.16}$$

and

$$M(\varphi) = \int_A E\left[\frac{u(\varphi)}{r} + \frac{1}{r}\frac{dv(\varphi)}{d\varphi} - \frac{r-R}{r}\left(\frac{1}{R}\frac{d^2u(\varphi)}{d\varphi^2} - \frac{1}{R}\frac{dv(\varphi)}{d\varphi}\right)\right](r-R)\, dA, \tag{A.17}$$

respectively. As for the evaluation of the integrals in Eqs. (A.16) and (A.17), it is noted that the axis of the arch is the line on which the centers of gravity of the cross-sections of the arch are located. The characteristic dimensions of the cross-section of a *slender* arch are very small compared with the radius of its axis. Consequently, the coordinate r, appearing in the denominator of the integrands in Eqs. (A.16) and (A.17), differs only very little from R. Therefore, it is admissible to set $r \approx R$ in the denominators of Eqs. (A.16) and (A.17). This results in the two constitutive equations, i.e. Eqs. (3) and (4). The relation between the stresses and the stress resultants follows from inserting Eq. (A.4) into Eq. (A.15), setting $r = R$ in the denominators of the resulting expression, and comparing the result with the Eqs. (3) and (4); see Eq. (8) for the result that is equal to the one derived in [35].

A.4. Virtual power of the internal forces

As for the virtual power of the internal forces, see Eq. (A.3), the stresses $\boldsymbol{\sigma}$ produce power on the Eulerian strain rate tensor, $\dot{\mathbf{d}}$, which, in the geometrically linearized theory, is equal to the rate of the virtual linearized strain tensor $\dot{\boldsymbol{\varepsilon}}$ [42,43,46]:

$$\mathcal{P}^{int} = -\int_V \boldsymbol{\sigma} : \dot{\boldsymbol{\varepsilon}}\, dV. \tag{A.18}$$

Virtual strain rates $\dot{\boldsymbol{\varepsilon}}$ are given, by analogy to the actual strain rates, as $\dot{\varepsilon}_{rr} = \dot{\varepsilon}_{zz} = \dot{\varepsilon}_{\varphi r} = \dot{\varepsilon}_{\varphi z} = \dot{\varepsilon}_{rz} = 0$, and

$$\dot{\varepsilon}_{\varphi\varphi}(r, \varphi, z; t) = \frac{\dot{u}(\varphi; t)}{r} + \frac{1}{r}\frac{\partial \dot{v}(\varphi; t)}{\partial \varphi}$$
$$- \frac{r-R}{r}\left(\frac{1}{R}\frac{\partial^2 \dot{u}(\varphi; t)}{\partial \varphi^2} - \frac{1}{R}\frac{\partial \dot{v}(\varphi; t)}{\partial \varphi}\right). \tag{A.19}$$

Consequently, $\boldsymbol{\sigma} : \dot{\boldsymbol{\varepsilon}} = \sigma_{\varphi\varphi} \dot{\varepsilon}_{\varphi\varphi}$. Hence, the virtual power of the internal forces reads, where considering the virtual strain rates, according to Eq. (A.19), as

$$\mathcal{P}^{int} = -\int_{\varphi_i}^{\varphi_f}\int_A \sigma_{\varphi\varphi}\left[\frac{\dot{u}(\varphi; t)}{r} + \frac{1}{r}\frac{\partial \dot{v}(\varphi; t)}{\partial \varphi}\right.$$
$$\left. - \frac{r-R}{r}\left(\frac{1}{R}\frac{\partial^2 \dot{u}(\varphi; t)}{\partial \varphi^2} - \frac{1}{R}\frac{\partial \dot{v}(\varphi; t)}{\partial \varphi}\right)\right] r\, dA\, d\varphi. \tag{A.20}$$

Substitution of Eqs. (A.12) and (A.14) into Eq. (A.20), and integration over the cross-sectional area, yields the following expression for the

virtual power of the internal forces in terms of normal forces and bending moments

$$\mathcal{P}^{int} = -\int_{\varphi_i}^{\varphi_f} N(\varphi)\left(\frac{\dot{u}(\varphi; t)}{R} + \frac{1}{R}\frac{\partial \dot{v}(\varphi; t)}{\partial \varphi}\right) R\, d\varphi$$
$$+ \int_{\varphi_i}^{\varphi_f} M(\varphi)\left(\frac{1}{R^2}\frac{\partial^2 \dot{u}(\varphi; t)}{\partial \varphi^2} - \frac{1}{R^2}\frac{\partial \dot{v}(\varphi; t)}{\partial \varphi}\right) R\, d\varphi. \tag{A.21}$$

A.5. Formulation of the principle of virtual power: equilibrium conditions

The equilibrium conditions for the stress resultants, see Eqs. (A.9)–(A.14), are obtained by means of the principle of virtual power, see Eq. (A.1). Specializing Eq. (A.1) for the virtual power of the external forces according to Eq. (A.8), and for the one of the internal forces according to Eq. (A.21), yields, after integration by parts and collection of similar terms,

$$\mathcal{P}^{ext} + \mathcal{P}^{int} = \int_{\varphi_i}^{\varphi_f}\left[-\frac{N(\varphi)}{R} + \frac{1}{R^2}\frac{d^2M(\varphi)}{d\varphi^2} + \frac{1}{R}\frac{dm(\varphi)}{d\varphi} + q_r(\varphi)\right]\dot{u}(\varphi; t)R\, d\varphi$$
$$+ \int_{\varphi_i}^{\varphi_f}\left[\frac{1}{R}\frac{dN(\varphi)}{d\varphi} + \frac{1}{R^2}\frac{dM(\varphi)}{d\varphi} + \frac{m(\varphi)}{R} + q_\varphi(\varphi)\right]\dot{v}(\varphi; t)R\, d\varphi$$
$$+ \left[V(\varphi) - m(\varphi) - \frac{1}{R}\frac{dM(\varphi)}{d\varphi}\right]\dot{u}(\varphi; t)\Big|_{\varphi_i}^{\varphi_f} = 0. \tag{A.22}$$

The principle of virtual power, see Eq. (A.22), must be satisfied for arbitrary admissible virtual velocity fields $\dot{u}(\varphi; t)$ and $\dot{v}(\varphi; t)$. This implies that the bracketed expressions in Eq. (A.22) must vanish, which results in the following equilibrium conditions

$$-\frac{N(\varphi)}{R} + \frac{1}{R^2}\frac{d^2M(\varphi)}{d\varphi^2} + \frac{1}{R}\frac{dm(\varphi)}{d\varphi} + q_r(\varphi) = 0, \tag{A.23}$$

$$\frac{1}{R}\frac{dN(\varphi)}{d\varphi} + \frac{1}{R^2}\frac{dM(\varphi)}{d\varphi} + \frac{m(\varphi)}{R} + q_\varphi(\varphi) = 0, \tag{A.24}$$

$$\frac{1}{R}\frac{dM(\varphi)}{d\varphi} + m(\varphi) = V(\varphi). \tag{A.25}$$

Finally, Eq. (A.25) is used to eliminate the bending moments in Eqs. (A.23) and (A.24). This yields the more familiar format of the equilibrium conditions of forces acting in the radial direction and the tangential direction, respectively, see Eqs. (5) and (6). Specializing Eq. (A.25) for $m(\varphi) = 0$ delivers the familiar format of the equilibrium conditions concerning bending moment and shear force, see Eq. (7).

Appendix B. Deformed configuration of the three-hinged arch, obtained by the unit force method

Since both the three-hinged arch and its dead load are symmetric, see Fig. 11, only one half of the arch needs to be considered, see Fig. B.1. The deformed configuration can be described by the two orthogonal displacement components $u_x(\varphi)$ and $u_y(\varphi)$. With the

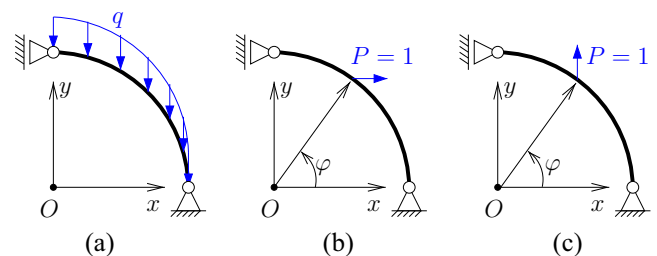

Fig. B.1. Illustration concerning the use of the unit force method for computation of the displacements: (a) one half of the three-hinged arch, (b) moving unit load in the horizontal direction, (c) moving unit load in the vertical direction.

help of a horizontal force $P = 1$, applied at φ, the unit force method delivers the horizontal displacement $u_x(\varphi)$ as

$$u_x(\varphi) = -\frac{qR^4}{8EI}\left[2\pi(\pi-2)\cos^2\varphi + 2(\pi+3)\cos\varphi\sin\varphi\right.$$
$$+ \sin\varphi\left(4\pi\varphi - 3\pi^2 + 3\pi\right)$$
$$\left.+ 4\pi\cos\varphi + 2\pi\varphi + 6\varphi - 6\pi\right] - \frac{qR^2}{8EA}\left[4\varphi\cos^2\varphi + 2\pi\sin^2\varphi\right.$$
$$\left.+ (1-\pi)(2\cos\varphi + \pi)\sin\varphi + 2\varphi(\pi-3)\right]. \tag{B.1}$$

By analogy, the vertical displacement $u_y(\varphi)$ is obtained as

$$u_y(\varphi) = -\frac{qR^4}{8EI}\left[2(\pi+3)\cos^2\varphi + 2(2\varphi-\pi)\cos\varphi\sin\varphi\right.$$
$$+ \left(4\pi\varphi - 3\pi^2 + 3\pi\right)\cos\varphi$$
$$\left.- 4\pi\sin\varphi - 2\varphi^2 + 2\pi\varphi + 3\pi^2 - 5\pi - 6\right] - \frac{qR^2}{8EA}\left[2(\pi-1)\sin^2\varphi\right.$$
$$\left.+ 2(\pi-2\varphi)\sin\varphi\cos\varphi + \pi(1-\pi)(\cos\varphi - 1) + 2\varphi(\pi-\varphi)\right]. \tag{B.2}$$

Appendix C. List of symbols

A	cross-sectional area of the arch
B	width of the cross-section of the arch
C	cross-sectional contour of the arch
$C_1, C_2, C_3, C_4, C_5, C_6$	integration constants in the solutions for the unloaded part of the arch
$\mathbf{e}_r, \mathbf{e}_\varphi, \mathbf{e}_z$	base vectors of the cylindrical coordinate system
$\dot{\mathbf{d}}$	Eulerian rate of deformation tensor
E	Young's modulus
E_c	Young's modulus of concrete
E_s	Young's modulus of steel
EA	extensional stiffness
$\widehat{EA}$	extensional stiffness, considering $R/r \not\approx 1$
EI	bending stiffness
$\widehat{EI}$	bending stiffness, considering $R/r \not\approx 1$
$\widehat{EK}$	coupling stiffness, considering $R/r \not\approx 1$
$\mathbf{f}$	vector of volume forces
f_r, f_φ, f_z	components of $\mathbf{f}$
H	height of the cross-section of the arch
I	second moment of the cross-sectional area
m	distributed bending moment
M	bending moment
M_h	bending moment at the hinge at the crown of the arch
M_i	bending moment at the initial cross-section of the arch
M^L	load integral for the bending moment
$\mathbf{n}$	unit normal vector
$\mathbf{n}_s$	unit normal vector at the point with the coordinate s
N	normal force
N_i	normal force at the initial cross-section of the arch
N^L	load integral for the normal force
P	point load imposed on the arch
P_r	radial component of P
P_φ	tangential component of P
$\mathcal{P}^{int}$	virtual power of the internal forces
$\mathcal{P}^{ext}$	virtual power of the external forces
q	dead load intensity of the arch
q_r	radial component of q
q_φ	tangential component of q
r	radial coordinate of the polar coordinate system
R	radius of the axis of the circular arch
s	arc-length measured along the contour of the cross-section
t	time
$\mathbf{T}$	vector of surface tractions
T_r, T_φ, T_z	components of $\mathbf{T}$
$\mathbf{u}$	displacement vector
u	radial component of $\mathbf{u}$
u_i	radial displacement at the initial cross-section
u_x	horizontal component of $\mathbf{u}$
u_y	vertical component of $\mathbf{u}$
u^L	load integral for radial displacements
$\dot{\mathbf{u}}$	virtual velocity vector
$\dot{u}, \dot{v}$	components of $\dot{\mathbf{u}}$
v	tangential component of $\mathbf{u}$
V	shear force
v_i	tangential displacement of the axis at the initial cross-section
v^L	load integral for the tangential displacements
V_i	shear force at the initial cross-section of the arch
V^L	load integral for the shear force
w	axial component of the displacement of the axis of the arch
x	horizontal coordinate of the Cartesian coordinate system
y	vertical coordinate of the Cartesian coordinate system
z	axial coordinate of the cylindrical coordinate system
δ	deflection at the crown of the arch
δ_y	deflection at the crown of the arch at the onset of yielding of steel
Δu_j	relative radial displacement at interfaces
Δv_j	relative tangential displacement at interfaces
$\Delta \theta_j$	relative cross-sectional rotation at interfaces
$\Delta \theta_h$	relative cross-sectional rotation at the hinge at the crown of the arch
ε_{rr}	normal strain in the r (radial)-direction
$\varepsilon_{\varphi\varphi}$	normal strain in the φ (tangential)-direction
ε_{zz}	normal strain in the z (axial)-direction
$\varepsilon_{r\varphi}\ (=\varepsilon_{\varphi r})$	shear strain in the r-φ plane
$\varepsilon_{\varphi z}\ (=\varepsilon_{z\varphi})$	shear strain in the φ-z plane
$\varepsilon_{zr}\ (=\varepsilon_{rz})$	shear strain in the z-r plane
$\dot{\boldsymbol{\varepsilon}}$	rate of the virtual linearized strain tensor
$\dot{\varepsilon}_{rr}$	virtual normal strain rate in the r (radial)-direction
$\dot{\varepsilon}_{\varphi\varphi}$	virtual normal strain rate in the φ (tangential)-direction

$\dot{\bar{\varepsilon}}_{zz}$	virtual normal strain rate in the z (axial)-direction
$\dot{\bar{\varepsilon}}_{r\varphi}\ (=\dot{\bar{\varepsilon}}_{\varphi r})$	virtual shear strain rate in the r-φ plane
$\dot{\bar{\varepsilon}}_{\varphi z}\ (=\dot{\bar{\varepsilon}}_{z\varphi})$	virtual shear strain rate in the φ-z plane
$\dot{\bar{\varepsilon}}_{zr}\ (=\dot{\bar{\varepsilon}}_{rz})$	virtual shear strain rate in the z-r plane
γ	central angle of the circular arch
$\boldsymbol{\sigma}$	Cauchy stress tensor
σ_{rr}	normal stress in the r (radial)-direction
$\sigma_{\varphi\varphi}$	normal stress in the φ (tangential)-direction
σ_{zz}	normal stress in the z (axial)-direction
$\sigma_{r\varphi}\ (=\sigma_{\varphi r})$	shear stress in the r-φ plane
$\sigma_{\varphi z}\ (=\sigma_{z\varphi})$	shear stress in the φ-z plane
$\sigma_{zr}\ (=\sigma_{rz})$	shear stress in the z-r plane
θ	cross-sectional rotation
θ_i	rotation of the initial cross-section
θ^L	load integral for the cross-sectional rotation
φ	angular coordinate of the polar coordinate system
φ_f	polar position of the final cross-section of the arch
φ_i	polar position of the initial cross-section of the arch
φ_p	polar position of a point load on the arch
φ_j	polar position of an interface on the segmented tunnel ring

References

[1] Liu X, Bai Y, Yuan Y, Mang HA. Experimental investigation of the ultimate bearing capacity of continuously jointed segmental tunnel linings. Struct Infrastruct Eng 2016;12(10):1364–79.
[2] Nishikawa K. Development of a prestressed and precast concrete segmental lining. Tunn Undergr Sp Tech 2003;18(2):243–51.
[3] Ding WQ, Peng YC, Yan ZG, Shen BW, Zhu HH, Wei XX. Full-scale testing and modeling of the mechanical behavior of shield TBM tunnel joints. Struct Eng Mech 2013;45(3):337–54.
[4] Salemi A, Esmaeili M, Sereshki F. Normal and shear resistance of longitudinal contact surfaces of segmental tunnel linings. Int J Rock Mech Min Sci 2015;77:328–38.
[5] Gladwell GM. Contact problems in the classical theory of elasticity. Springer Science & Business Media; 1980.
[6] Janssen P. Tragverhalten von Tunnelausbauten mit Gelenktübbings [Load carrying behavior of segmented tunnel linings] [Ph.D. thesis]. Technische Universität Carolo-Wilhelmina, in German;1983.
[7] Altenburg A. The influence of number of segments due to the crosssectional forces [Ph.D. Graduation project]. Delft University of Technology; 1997.
[8] Li X, Yan Z, Wang Z, Zhu H. A progressive model to simulate the full mechanical behavior of concrete segmental lining longitudinal joints. Eng Struct 2015;93:97–113.
[9] Zhang W, Jin X, Yang Z. Combined equivalent & multi-scale simulation method for 3-D seismic analysis of large-scale shield tunnel. Eng Comput 2014;31(3):584–620.
[10] Majdi A, Ajamzadeh H, Nadimi S. Investigation of moment-rotation relation in different joint types and evaluation of their effects on segmental tunnel lining. Arabian J Geosci 2016;9(7):1–15.
[11] Blom CBM. Design philosophy of concrete linings for tunnels in soft soils [Ph.D. thesis]. Delft University of Technology; 2002.
[12] Nakamura H, Kubota T, Furukawa M, Nakao T. Unified construction of running track tunnel and crossover tunnel for subway by rectangular shape double track cross-section shield machine. Tunn Undergr Sp Tech 2003;18(2):253–62.
[13] Luttikholt A. Ultimate limit state analysis of a segmented tunnel lining [Master thesis]. Delft University of Technology; 2007.
[14] Lu L, Lu X, Fan P. Full-ring experimental study of the lining structure of Shanghai Cangjiang tunnel. J Civil Eng Archit 2011;5(8):732–9.
[15] Zhong X, Zhu W, Huang Z, Han Y. Effect of joint structure on joint stiffness for shield tunnel lining. Tunn Undergr Sp Tech 2006;21(3):406–7.
[16] Wood AM. The circular tunnel in elastic ground. Geotech 1975;25(1):115–27.
[17] Lee K, Ge X. The equivalence of a jointed shield-driven tunnel lining to a continuous ring structure. Can Geotech J 2001;38(3):461–83.
[18] Hefny A, Tan F, Macalevey N. Numerical study on the behaviour of jointed tunnel lining. J Inst Eng 2004;44(1):108–18.
[19] Hefny AM, Chua H-C. An investigation into the behaviour of jointed tunnel lining. Tunn Undergr Sp Tech 2006;21(3):428.
[20] Mashimo H, Ishimura T. Evaluation of the load on shield tunnel lining in gravel. Tunn Undergr Sp Tech 2003;18(2):233–41.
[21] Lee K, Hou X, Ge X, Tang Y. An analytical solution for a jointed shield-driven tunnel lining. Int J Numer Anal Meth Geomech 2001;25(4):365–90.
[22] Koyama Y. Present status and technology of shield tunneling method in Japan. Tunn Undergr Sp Tech 2003;18(2):145–59.
[23] Teachavorasinskun S, Chub-uppakarn T. Influence of segmental joints on tunnel lining. Tunn Undergr Sp Tech 2010;25(4):490–4.
[24] Do N-A, Dias D, Oreste P, Djeran-Maigre I. 2D numerical investigation of segmental tunnel lining behavior. Tunn Undergr Sp Tech 2013;37:115–27.
[25] Do N-A, Dias D, Oreste P, Djeran-Maigre I. Three-dimensional numerical simulation for mechanized tunnelling in soft ground: the influence of the joint pattern. Acta Geotech 2014;9(4):673–94.
[26] Hellmich C, Mang HA, Ulm F-J. Hybrid method for quantification of stress states in shotcrete tunnel shells: combination of 3D in situ displacement measurements and thermochemoplastic material law. Comput Struct 2001;79(22):2103–15.
[27] Ullah S, Pichler B, Scheiner S, Hellmich C. Shell-specific interpolation of measured 3D displacements, for micromechanics-based rapid safety assessment of shotcrete tunnels. Comput Model Eng Sci (CMES) 2010;57(3):279–315.
[28] Ullah S, Pichler B, Hellmich C. Modeling ground-shell contact forces in NATM tunneling based on three-dimensional displacement measurements. J Geotech Geoenviron Eng 2013;139(3):444–57.
[29] Hellmich Ch, Macht J, Mang HA. Ein hybrides Verfahren zur Bestimmung der Auslastung von Spritzbetonschalen [A Hybrid Method for Determination of the Degree of Utilization of Shotcrete Tunnel Shells]. Felsbau 1999;17(5):422–5 [In German].
[30] Zhao H, Liu X, Bao Y, Yuan Y, Bai Y. Simplified nonlinear simulation of shield tunnel lining reinforced by epoxy bonded steel plates. Tunn Undergr Sp Tech 2016;51:362–71.
[31] Park R, Paulay T. Reinforced concrete structures. John Wiley & Sons; 1975.
[32] Dym CL, Williams HE. Stress and displacement estimates for arches. J Struct Eng 2011;137(1):49–58.
[33] Sanders JL. Nonlinear theories for thin shells. Q Appl Math 1963;21:21–36.
[34] Love AEH. A treatise on the mathematical theory of elasticity. 2nd ed. Cambridge University Press; 1906.
[35] Melan J. Theory of arches and suspension bridges. Chicago: Clark; 1913.
[36] H. Rubin, U. Vogel, Baustatik ebener Stabwerke [Frameworks for structural analysis], Stahlbau Handbuch Für Studium und Praxis BAND 1Teil A, Stahlbau-Verlagsgesellschaft mbH, Köln; 1993 [In German].
[37] La Poutré D, Spoorenberg R, Snijder H, Hoenderkamp J. Out-of-plane stability of roller bent steel arches – an experimental investigation. J Constr Steel Res 2013;81:20–34.
[38] Guo Z, Wang Y, Lu N, Zhang H, Zhu F. Behaviour of a two-pinned steel arch at elevated temperatures. Thin Walled Struct 2016;107:248–56.
[39] CEN. European Committee for Standardisation, EN 1993-1-11 (2006) (English): Eurocode 3: Design of steel structures – Part 1-11: Design of structures with tension components. London; 2006.
[40] Mentrasti L. Bending of large curvature beams. I. Stress method approach. Int J Solids Struct 2001;38(32):5703–26.
[41] Zhang H, Liu X, Yuan Y. Non-linear mechanical analysis of shield tunnel structure at ultimate loading. In: Bicanic N, Mang H, Borst R de, editors. Proceedings of the EURO-C 2014 conference on computational modelling of concrete structures, vol. 2. Leiden, St. Anton am Arlberg, Austria: Taylor and Francis Group; 2014. p. 893–8.
[42] Germain P. The method of virtual power in continuum mechanics. Part 2: Microstructure. SIAM J Appl Math 1973;25(3):556–75.
[43] Frémond M, Nedjar B. Damage, gradient of damage and principle of virtual power. Int J Solids Struct 1996;33(8):1083–103.
[44] Del Piero G. On the method of virtual power in continuum mechanics. J Mech Mater Struct 2009;4(2):281–92.
[45] Maugin GA. The principle of virtual power: from eliminating metaphysical forces to providing an efficient modelling tool. Continuum Mech Thermodyn 2013;25(2):127–46.
[46] Salençon J. Handbook of continuum mechanics: general concepts-thermoelasticity. Springer; 2001.